

A New Technique for Spectral Analysis of Ionospheric TEC Fluctuations Observed with the Very Large Array VHF System: From QP Echoes to MSTIDs

J. F. Helmboldt,¹ T. J. W. Lazio,² H. T. Intema,³ & K. F. Dymond,¹

We have used a relatively long, contiguous VHF observation of a bright cosmic radio source (Cygnus A) with the Very Large Array (VLA) through the nighttime, midlatitude ionosphere to demonstrate the phenomena observable with this instrument. In a companion paper, we showed that the VLA can detect fluctuations in total electron content (TEC) with amplitudes of $\leq 10^{-3}$ TECU and can measure TEC gradients with a precision of about 2×10^{-4} TECU km⁻¹. We detail two complementary techniques for producing spectral analysis of these TEC gradient measurements. The first is able to track individual waves with wavelengths of about half the size of the array (~ 20 km) or more. This technique was successful in detecting and characterizing many medium-scale traveling ionospheric disturbances (MSTIDs) seen intermittently throughout the night and has been partially validated using concurrent GPS measurements. Smaller waves are also seen with this technique at nearly all times, many of which move in similar directions as the detected MSTIDs. The second technique allows for the detection and statistical description of the properties of groups of waves moving in similar directions with wavelengths as small as 5 km. Combining the results of both spectral techniques, we found a class of intermediate and small scale waves which are likely the quasi-periodic (QP) echoes that have been observed to occur within sporadic-*E* (E_s) layers. We find two distinct populations of these waves. The members of one population are coincident in time with MSTIDs and are consistent with being generated within E_s layers by the $E-F$ coupling instability. The other population seems more influenced by the neutral wind, similar to the predominant types of QP echoes found by the Sporadic-*E* Experiments over Kyushu [SEEK *Fukao et al.*, 1998; *Yamamoto et al.*, 2005]. We have also found that the spectra of background (i.e., isotropic) fluctuations can be interpreted as the sum of two turbulent components with maximum scales of about 300 km and 10 km.

1. Introduction

Ground-based remote sensing of the ionosphere is a rich field of study that has developed over several decades and now includes a host of different instruments including, but not limited to, GPS, CERTO [Bernhardt and Siefring, 2006], and other radio beacon receivers, ionosondes, and radar/HF arrays. A

powerful yet relatively underused resource for remote sensing are radio-frequency arrays, particularly those that operate in the VHF regime. Designed as radio synthesis telescopes, they are chiefly used to observe cosmic sources. While such observations require detailed calibration schemes to remove the effects of the ionosphere, this calibration data is seldom used to actually study the ionosphere.

These interferometers basically measure the time-averaged correlation of complex voltages from pairs of antennas which can be combined with Fourier methods to make relatively high angular resolution images of cosmic sources [for a detailed discussion of the methods involved, see *Thompson et al.*, 1991]. The correlated signals, or “visibilities” have an extra phase term added to them by the ionosphere proportional to the difference in the total electron content (TEC) between the two antennas’ lines of

¹US Naval Research Laboratory, Washington, DC, USA.

²Jet Propulsion Laboratory, California Institute of Technology, Pasadena, CA, USA.

³Jansky Fellow of the National Radio Astronomy Observatory, Charlottesville, VA, USA.

sight. Because of the relatively large collecting area of the individual elements (usually dishes, dozens of meters across), and the brightness of many cosmic sources, these additional phase terms can typically be converted to differential TEC (δTEC) measurements with a precision of $\sim 10^{-3}$ TECU or better. In addition, the range of scales that can be probed with such interferometers (dozens of meters to hundreds of kilometers) and the virtual ubiquity of target sources available on the sky make them valuable assets for the exploration of ionospheric dynamics from very fine to medium size scales.

Consequently, radio arrays have been used, to a somewhat limited degree, for ionospheric studies. Because of the relative stability of its electronics, quiet radio frequency interference (RFI) environment, and available VHF system (bands at 74 and 330 MHz), the Very Large Array (VLA) has been used almost exclusively in these efforts. Seminal experiments were performed by *Jacobson and Erickson* [1992a, b] using 330 MHz VLA observations of several sources to explore the environment of ionospheric waves above the VLA. Among other results, they discovered a new class of magnetic eastward directed waves that were later shown to actually be located within the plasmasphere [*Hoogeveen and Jacobson*, 1997]. Subsequent larger-scale investigations using data from the VLA Low-frequency Sky Survey [VLSS; *Cohen et al.*, 2007], a survey of the northern sky at 74 MHz, have shown that the median behavior of ionospheric fluctuations observed by the VLA over several years is essentially consistent with turbulence [*Cohen and Röttgering*, 2009]. Joint observations made with an all-sky optical camera and the VLA at 74 and 330 MHz by *Coker et al.* [2009] demonstrated the VLA’s ability to aid in the exploration of the interaction between gravity waves generated lower in the atmosphere and relatively small-scale phenomena such as sporadic-*E*. Recently, from a campaign using the VLA and the COSMIC satellite, *Dymond et al.* [2011] were able to detect a relatively rare instance of a southeastward-propagating traveling ionospheric disturbance (TID).

In a companion paper [*Helmboldt et al.*, 2011], we described in detail the methods for extracting ionospheric information from the calibration of VLA VHF system data. We demonstrated that when observing a bright cosmic source, the VLA VHF system was capable of achieving a typical δTEC precision of 3×10^{-4} TECU. Since arrays such as the VLA are es-

entially only sensitive to the TEC gradient, we also detailed techniques for measuring time series of the TEC gradient to a precision of about 2×10^{-4} TECU km^{-1} . Here, we seek to develop this effort further by presenting new spectral analysis techniques for these TEC gradient measurements. We will demonstrate that these techniques are capable of detecting and characterizing several phenomena from medium (~ 100 km) to small (~ 5 km) scales while also providing a broader statistical description of the spectrum of TEC fluctuations observable with the VLA.

2. Observations and TEC Gradient Measurements

The data used in this analysis came from a roughly 12-hour VLA observation of one of the brightest cosmic radio sources, Cygnus A (or “Cyg A”; also known as 3C405) from a latitude and longitude of $34^\circ 04' 43.497''$ N and $107^\circ 37' 05.819''$ W (VLA program number AK570). The observations were conducted during the night of 12-13 August, 2003 simultaneously at 74 and 327 MHz, both operating in dual polarization. The VLA was in its “A” configuration spanning a circle with a diameter of about 40 km. The observations consisted of a 35-minute block of time, or “scan,” and a second 12-hour scan with a temporal sampling of 6.67 seconds. There was a moderate amount of geomagnetic activity (K_p index $\approx 2-4$) and the amount of solar activity was fairly average ($F10.7 = 123$ SFU).

Measurements of the TEC gradient toward Cyg A are described in detail in *Helmboldt et al.* [2011]. In short, the ionosphere adds an extra phase term to the complex visibility measure for each pair of antennas which is proportional to the difference in the TEC along the two lines of sight, or δTEC . Thus, the interferometer is sensitive only to TEC gradients and not absolute TEC. However, the Y-shape of the array (northern, southeastern, and southwestern “arms”) makes measuring and performing Fourier inversions of the TEC gradient difficult. This is in contrast to the standardized procedure of inverting visibilities to produce images of cosmic sources. This is because the visibilities are functions of the *differential* antenna positions and the TEC gradient is a function of the *actual* antenna positions projected through the ionosphere. This is discussed in more detail by *Helmboldt et al.* [2011].

Because of the consequences of the Y-shape of the VLA, *Helmboldt et al.* [2011] established two ad hoc

approaches to measuring the TEC gradient. The first method estimates the full two-dimensional gradient at each antenna using a second-order, two-dimensional polynomial (Taylor series) on each time step. While insensitive to fine-scale structure significantly smaller than the array, *Helmboldt et al.* [2011] showed that this method is effective in recovering the gradient associated with relatively large, long-period disturbances visible at dusk, dawn, and intermittently throughout the night.

The second method numerically computes the projection of the TEC gradient along each of the VLA arms at each antenna and time step. While little directional information can be obtained with these measurements, *Helmboldt et al.* [2011] showed that there are many significant fine-scale fluctuations, especially near midnight local time, that are detected with this method and missed/damped within the polynomial-based method. In the following section, we will detail the techniques we have developed to spectrally analyze the TEC gradient time series produced by these two methods.

3. Spectral Analysis

3.1. Method

To identify individual disturbances or sets of disturbances that passed over the array, we have developed the following Fourier-based method which uses the polynomial-based TEC gradient measurements. This method is partially based on that used by *Jacobson and Erickson* [1992a], but expands upon it to include some allowance for wavefront distortions and multiple wave fronts observed simultaneously.

The basic concept is to use both the apparent motion of Cyg A and the movements of the observed ionospheric disturbances to increase the spatial coverage of the VLA. In other words, we will essentially convert temporal baselines into spatial ones, sampling the observed phenomena with a relatively long, 40 km-wide “strip.” Since there are presumably several disturbances contributing to the TEC gradient at each time step with a range of speeds, the temporal sampling cannot be converted into the same set of spatial samples for all observed phenomena. Instead, we must separate the time series for each antenna into different Fourier modes and then analyze how the properties of each mode vary across the array to

estimate the wavelength, speed, and direction of the contributing pattern(s).

To achieve this, we first assumed that the TEC fluctuations could be approximated as the sum of many individual oscillating modes, each having the following form

$$\text{TEC}(t) = A(r_{\perp}) \exp \left[i \left(-\vec{k} \cdot \vec{r} + 2\pi\nu t \right) \right] \quad (1)$$

where \vec{k} and \vec{r} are the wavenumber and position vectors, respectively, $A(r_{\perp})$ is a complex amplitude which only varies perpendicular to \vec{k} (i.e., wavefront distortions), and the temporal frequency, ν , is assumed to be $= v|\vec{k}|/(2\pi)$ where v is the wave speed. For a single Fourier mode with temporal frequency, ν , the Fourier transforms of the x (N-S) and y (E-W) partial derivatives are given by

$$F_x(\nu) \simeq \left[ik_{\nu,x} + \frac{\partial}{\partial x} A_{\nu}(r_{\perp}) \right] e^{-i\vec{k}_{\nu} \cdot \vec{r}} \quad (2)$$

$$F_y(\nu) \simeq \left[ik_{\nu,y} + \frac{\partial}{\partial y} A_{\nu}(r_{\perp}) \right] e^{-i\vec{k}_{\nu} \cdot \vec{r}} \quad (3)$$

From these equations, one can see that along a line parallel to \vec{k} , the x and y dependences of the phases of F_x and F_y are identical since both partial derivatives of $A_{\nu}(r_{\perp})$ are constant along this line. There may be other lines in the x, y plane where this is true. For instance, in the absence of significant wavefront distortions, the x and y dependencies will be the same everywhere. However, in the general case, the line parallel to \vec{k} is the only one where these dependencies are required to be equal according to equations (2) and (3). We have exploited this fact in our analysis to help determine the direction of \vec{k} for different Fourier modes and consequently, the wavenumbers and velocities.

To illustrate this better, we have displayed an example of a wave, including wavefront distortions, in Fig. 1. If one imagines this wave drifting over the VLA at a constant speed, one can see that the time series measured at two separate points will have identical periods, but will be out of phase. For a constant speed, this phase difference will simply be proportional to the length of the separation between the points. However, if one examines the N-S and E-W partial derivatives of this wave along different position vectors, one can see that the wavefront distortions add additional variations in phase. We show this in the lower panels of Fig. 1 where we have plotted the N-S and E-W partial derivatives, F_x and F_y , along three different vectors shown on the image of

the wave with color-coded arrows. In all cases, F_x and F_y are out of phase with one another. This phase difference is constant for the vector that is parallel to the wavenumber vector but varies with distance along the other two vectors. Therefore, when wavefront distortions are present, the time series phases will have the same spatial derivative for both F_x and F_y only when points along the direction of the wave are considered.

While this derivation focuses on what one should expect for a single wave pattern, we must recognize that at a given temporal frequency, ν , there will likely be contributions from several waves. This can result from several factors including the finite size of the temporal window used for the Fourier inversion to the existence of phenomena such as turbulent cascades which have distributions of spectral power that span a large range of frequencies. In this case, wave properties derived for a single mode using equations (2) and (3) will be weighted mean¹ values with more weight given to larger amplitude fluctuations. In addition, even for a single dominant wave, the actual wavenumber and speed for a particular value of ν may change over the span of time used in the Fourier inversion. Therefore, one should take the measured values for these properties to be averages over either the temporal window used for the Fourier transforms or the duration of the disturbance(s), whichever is shorter.

Thus, we may identify instances where single dominant waves are present by deriving wave properties using equations (2) and (3) for several temporal frequencies at each time step. This can be done using Fourier transforms computed with a “sliding” window, one that is relatively wide but centered on each individual time step. The derived spectral power, direction, and speed can then be examined as functions of time and ν . Any relatively large regions in the t, ν plane with relatively large power and uniform direction and speed are likely instances of dominant waves. The wave properties measured in all other locations in the t, ν plane are likely composite values from several waves and can be used to study wave properties on a statistical basis.

3.2. Derived Wave Properties

Using the polynomial-based TEC gradient fits, we calculated F_x and F_y from equations (2) and (3) as functions of time by computing the discrete Fourier transform (DFT) of each polynomial coeffi-

cient within one-hour sliding windows for frequencies up to 12 hr^{-1} (or, periods > 5 minutes). We chose the one-hour width because it was the same used to de-trend the δTEC data [see *Helmboldt et al.*, 2011]. Because of the one-hour box width, we excluded the first 35 minute scan from this analysis. We also only computed F_x and F_y for times ranging from one half hour after the beginning of the second scan to one half hour before the end of the observing run so that a full hour of data could be used for each time step.

The DFT of each polynomial coefficient was then used to compute F_x and F_y at the locations of the antennas where the values of the polynomial fits are most reliable. Upon inspection of this data, we found that the phases of both F_x and F_y at a single value of ν were typically well approximated with planes across the array. Because of this, at each time step and value of ν , we fit planes to both these quantities. We then checked the combined (in quadrature) rms scatter about both of these fits against the rms difference between the phases of F_x and F_y to see if the x and y dependencies of these phases indeed differed across the array, indicating significant wavefront distortions. In the vast majority ($> 97\%$) of cases, the rms difference between the phases of the two partial derivative DFTs was larger than the combined rms scatter about the two planar fits (a median of four times larger). In these cases, we assumed that the azimuth angle (measured clockwise from north) of the line where the two planes intersected was the azimuth angle of \vec{k} and that the derivative of the DFT phase along this line gave $|\vec{k}|$. In the rare instance that there was no evidence of wavefront distortions, we computed a mean x and y slope for the DFT phases from the two planar fits and computed the direction and magnitude of \vec{k} from these slopes.

The upper panel of Fig. 2 displays the total power of the TEC gradient in the direction of \vec{k} as a function of local time and temporal frequency. While seemingly random fluctuations are frequently apparent, there are several instances where one can see significant detections of waves above the background. Most of these waves are seen between frequencies of 1 and 5 hr^{-1} , or periods of 12 to 60 minutes. This is roughly consistent with what is typical for MSTIDs. To isolate these detections, we computed a mask by measuring the median and median absolute deviation (MAD) within elliptical “annuli” around each pixel that had dimensions of 1.5 hr in local time by 3 hr^{-1} in ν . Any pixel with a value more than three times the MAD above the median for its annulus was con-

sidered a detection above the background. We used this mask to display both the azimuth angle for \vec{k} and the wave speed for significant detections in the middle and lower panels of Fig. 2, respectively.

The plots in Fig. 2 imply that the candidate MSTIDs, i.e. fluctuations with periods ~ 20 minutes or greater, have estimated speeds between 100 and 200 m s^{-1} , consistent with typical MSTIDs detected at night during northern hemisphere summer [Hernández-Pajares *et al.*, 2006]. They also appear to move roughly westward/northwestward before midnight and toward the northeast after midnight. While Tsugawa *et al.* [2007] showed that summer nighttime MSTIDs in the northern hemisphere predominantly move toward the southwest, Hernández-Pajares *et al.* [2006] showed that near the west coast in California, they move almost due west and occasionally toward the northwest. Thus, the waves observed before midnight are somewhat typical MSTIDs. However, the northeastward directed waves seen after midnight are unusual and will be discussed in more detail below.

3.3. Mean Power Spectra

While the results displayed in Fig. 2 are useful for identifying and examining instances of waves or groups of waves, the polynomial-based analysis can also be used to produce a more statistical description of the observed set of TEC fluctuations. In Fig. 3, we have plotted the mean power within bins of wavenumber, k , for one-hour blocks of time. We note that these wavenumbers have not been corrected for any Doppler shifts caused by the motion of the ionosphere pierce-points as the VLA tracked the apparent motion of Cyg A through the sky. However, the results shown in Appendix A of Helmboldt *et al.* [2011] demonstrated that the equivalent velocities at the estimated peak heights for the pierce-points are relatively small ($\sim 20 \text{ m s}^{-1}$), except near the beginning and end of the observing run when Cyg A was rising and setting. At these times, the main features detected in the data shown in Fig. 2 generally move roughly perpendicular to the pierce-point motions, implying that the Doppler shifts were relatively small during these times as well.

We have also plotted in Fig. 3 what we will refer to as “noise-equivalent” spectra. These spectra were computed by performing the polynomial fits to each of the four δTEC measurements (two bands and two polarizations) and computing the DFT of the dif-

ference between those fits and the fits to the final δTEC . The wave analysis detailed above was then applied to these residual DFTs to estimate the results one would achieve if analyzing fluctuations that were simply noise. The noise-equivalent spectra plotted in Fig. 3 are average spectra computed within each one-hour block and among the two bands and two polarizations.

These spectra imply that this technique can indeed detect significant power of structures as small as about half the size of the array (or, $k \approx 0.3 \text{ km}^{-1}$). The MSTIDs visible in the upper panel of Fig. 2 are visible in most of the panels as significant bumps above the background at wavenumbers ranging from 0.015–0.05 km^{-1} , or wavelengths of about 130–500 km, which is again roughly consistent with the known properties of MSTIDs. Few if any features are seen at higher wavenumbers where the spectrum ranges from a simple power-law, reminiscent of turbulence, to relatively flat spectra, which may imply a population of intermediate-scale waves.

To explore these data further, we have computed mean power spectra within bins of \vec{k} azimuth angle. We have displayed these as images in Fig. 4 where we have divided the data within the same wavenumber bin by the total power within that bin over all azimuth angles to enhance any detected features at higher wavenumbers. These images reveal that there are often intermediate-scale waves ($k > 0.1 \text{ km}^{-1}$, or wavelengths $< 60 \text{ km}$) detected moving in some preferred direction. Often, these waves appear to be moving in directions similar to detected MSTIDs. This is especially apparent in the first three panels where one can see that even when the MSTIDs have disappeared by a local time of -04^{h} , the roughly northward moving intermediate-scale waves persisted. The presence of strong MSTIDs do not appear to be required for these intermediate-scale waves as they seem to exist during all time periods. However, the MSTIDs broadly appear to have the effect of “focussing” the intermediate-scale waves into a particular direction.

Those smaller-scale waves which are directed parallel to coincident MSTIDs may simply be small-scale structures within the MSTIDs themselves. Indeed, our spectral analysis method has indicated that significant wavefront distortions are common within the VLA data. However, the smaller waves which do not travel in the same direction as MSTIDs may be located within the E region, most likely within sporadic- E (E_s) layers given the prevalence

of this phenomenon during summer nighttime. In fact, *Coker et al.* [2009] showed that E_s layers are likely the source of small-scale TEC fluctuations often observed with the VLA during summer nighttime. In addition, ~ 10 -km-sized wave-like fluctuations have frequently been observed within E_s layers as so-called quasi-periodic (QP) echoes [e.g., *Fukao et al.*, 1998; *Yamamoto et al.*, 2005]. If so, these waves may yield further insights into the coupling between the midlatitude nighttime E and F layers [see *Cosgrove and Tsunoda*, 2004; *Cosgrove et al.*, 2004] as the MSTIDs are likely located within the lower F region [see, e.g., *Hernández-Pajares et al.*, 2006]. This will be discussed further in §5.

3.4. Contemporaneous GPS and Ionosondes Data

3.4.1. GPS Data

To partially validate our technique for detecting and characterizing waves, we have analyzed all available GPS data in the area for the time of our observations. From 12–13 August, 2003, there were six dual frequency GPS receivers operating within the state of New Mexico (station codes AZCN, NMSF, PIE1, SC01, TCUN, and WSMN) with publicly available data in RINEX format. In contrast, there are currently more than 30 such stations in operation which bodes well for future studies conducted with the new VHF system being developed for the Expanded VLA (EVLA). Data for each of the six stations operating in 2003 were obtained and processed with standard GPS Toolkit [*Tolman et al.*, 2004] routines (`DiscFix` and `ResCor`) to produce slant and vertical (for a height of 400 km) relative TEC values (i.e., no bias correction was done) for all available satellites.

For each station/satellite pair, the slant TEC data were de-trended according to *Hernández-Pajares et al.* [2006] where they de-trended similar data by subtracting from each time step the average of two values, each an interval τ before or after the time step. They noted that for a wave with a period T , this technique effectively multiplies the wave amplitude by a factor of $2 \sin^2(\pi\tau/T)$. They chose a value of $\tau = 300$ s based on physical arguments of the expected periods of MSTIDs. We have instead chosen $\tau = 600$ s so that the de-trending technique was optimized for waves with periods similar to the MSTIDs detected within our VLA data.

After the GPS data were de-trended, they were corrected to vertical TEC values using the corrections computed by `ResCor` within GPS Toolkit. Within two-hour blocks, starting at a local time (rel-

ative to midnight, 13 August) of -06^{h} , we then identified station/satellite pairs which had relatively contiguous data ($> 90\%$ of the time interval covered) from one half hour before and one half hour after the time block. We then computed the DFT of the de-trended TEC data within a one-hour sliding window to produce a spectrum at each time step within the two-hour block.

These spectra are displayed in Fig. 5 within each two-hour block for the 12 station/satellite pairs with ionospheric “pierce-points” closest to that associated with Cyg A. Nearly all of these spectra show some level of wave activity with periods of about 12–60 minutes ($\nu = 1\text{--}5 \text{ hr}^{-1}$). Those station/satellite pairs with pierce-points closest to that of Cyg A in particular show very good agreement with the VLA-derived spectrum displayed in the upper panel of Fig. 2. This is especially true for the top three rows of Fig. 5 for local times of -06^{h} to -04^{h} and 01^{h} to 03^{h} .

Unfortunately, the spacing among the GPS stations was too large to be able to track individual waves. The closest separations among pierce-points is > 100 km when separations on the order of tens of kilometers are required to overcome the effects of wavefront distortions [e.g., *Hernández-Pajares et al.*, 2006]. This makes it difficult to use the GPS data to directly validate the directional information we have determined for the VLA-detected waves displayed in the middle panel of Fig. 2. However, the fact that the spectra shown in Fig. 2 and 5 observe many of the same waves is encouraging and at least partially validates our VLA-based approach.

3.4.2. Ionosondes Data

While there were no ionosondes operating in the immediate vicinity of the VLA, there were two relatively nearby at similar latitudes, one at Dyess Air Force Base (AFB) in west Texas ($32^\circ 30'' \text{ N}$; $99^\circ 42' \text{ W}$), and one at Point Arguello in California ($35^\circ 36'' \text{ N}$; $120^\circ 36' \text{ W}$). The contemporaneous data from these stations are useful for interpreting our VLA observations.

For instance, northward or northeastward-directed MSTIDs, similar to those observed here at $01^{\text{h}}\text{--}03^{\text{h}}$ and $04^{\text{h}}\text{--}04^{\text{h}}30^{\text{m}}$, have been observed over Japan with the SuperDARN Hokkaido HF radar and an airglow imager by *Shiokawa et al.* [2008]. Like the northeastward-directed MSTIDs described here, these were detected at midlatitudes during nighttime. *Shiokawa et al.* [2008] noted that the roughly northward-directed MSTIDs were observed with the

SuperDARN array most frequently in May and August. They also noted that the northeastward-directed waves were coincident in time with a drop in the height of the F-region as indicated with nearby ionosondes data.

To demonstrate that this may also be the case for our VLA observations, we have plotted h'F for both the Dyess AFB and Point Arguello ionosondes as functions of VLA local time in the upper panel of Fig. 6. The Point Arguello data show a substantial drop in h'F at around 01^h at the start of the first observed instance of northeastward directed waves. The Dyess AFB data shows a decline in h'F which begins around 02^h and reaches a minimum at about 04^h30^m, corresponding to the middle of the second period of northeastward MSTID activity. This indicates that it is plausible that we have observed a similar phenomenon with VLA over New Mexico as was found by *Shiokawa et al.* [2008] over Japan.

The ionosondes data also serve to validate our claims that E_s layers were present during our observations. In the lower panel of Fig. 6, we have plotted foEs for both ionosondes stations. Both stations observed E-region reflections with maximum frequencies between 2 and 6 MHz throughout the night, strongly indicating that E_s layers were present. The most active time for the appearance of these layers seems to be between $-02^{\text{h}}30^{\text{m}}$ and $04^{\text{h}}30^{\text{m}}$ VLA local time, especially for the Point Arguello station. As evidenced by Fig. 3 and 4, relatively small-scale fluctuations are visible within the VLA data throughout this time period. They are especially prominent from -02^{h} to 01^{h} where their presence has made the mean spectra shown in Fig. 3 virtually flat for wavenumbers $>0.13 \text{ km}^{-1}$.

4. Statistical Wave Properties

4.1. Arm-based Spectra

While the Fourier analysis detailed in §3 has yielded interesting results, it neglects the ability of the VLA in its A configuration to detect fluctuations on scales as small as a few kilometers. To make full use of the data, we have developed a complementary spectral analysis which uses the projected TEC gradients measured along each arm which are sensitive to fluctuations with sizes as small as the shortest antenna spacings within the VLA.

To analyze the projected gradients in a manner similar to the method used for the polynomial-based

gradients, we first performed fast Fourier transforms (FFTs) of the times series for each antenna. This was done within a sliding window of approximately one hour (512 time steps, or 56.9 minutes) centered on each time step. Then, for a single arm, time step, and temporal frequency, we unwrapped the phases of the FFTs along the arm and numerically computed the derivatives of these phases with respect to distance along the arm to obtain estimates of the (mean) projected wavenumber, k_{proj} , of each Fourier mode. As noted in §3, our Fourier analysis of the polynomial fits revealed that significant wavefront distortions were common. Because of this, we expect that these k_{proj} estimates are not reliable for tracking individual disturbances along any of the arms. However, since the effects of such distortions should average to zero over time, these estimates are sufficient to perform a statistical analysis of the overall population of waves seen by the VLA from a few to hundreds of kilometers in wavelength.

To begin such a statistical analysis, we binned the FFT and k_{proj} data within one-minute intervals and computed the mean FFT power within bins of k_{proj} for each arm. The resulting spectra are displayed in Fig. 7 where positive projected wavenumbers correspond to directions outward from the center of the array, or “up” the arm and negative projected wavenumbers correspond to inward directions, or “down” the arm. Since these are projected wavenumbers, instances where there are groups of waves moving in a particular direction will show up in these plots as over-densities in the positive (negative) direction for one arm, and in the negative (positive) direction for the other two. In cases where a group of waves moves nearly perpendicular to a particular arm, they will not show up at all in that arm’s spectrum. A good example of this can be seen between roughly 02^h and 03^h local time (highlighted with vertical white lines in the panels of Fig. 7). Here, there is an obvious over-density on the positive side of the spectrum for the southwestern arm and mild over-densities on the negative sides of the spectra for the northern and southeastern arms. This implies that these fluctuations are moving almost directly toward the southwest. Part of this group of waves can also be seen the panel of the upper right corner of Fig. 4, but in Fig. 7, they can be seen to extend to wavenumbers of at least 0.7 km^{-1} , or wavelengths at least as small as 9 km.

To establish the minimum scales on which this analysis can be considered reliable, we have also com-

puted noise-equivalent spectra using the full two-band, two-polarization data as we did with the polynomial-based Fourier analysis in §3. We have plotted in Fig. 8 mean spectra for each arm within one hour blocks of time along with the corresponding noise-equivalent spectra. In some instances, the spectra are always above the noise-equivalent spectra. However, in general, the spectra reach the noise level at projected wavelengths of about 5 km, or $k_{proj} = \pm 1.26 \text{ km}^{-1}$ (see the vertical dotted lines in Fig. 8). This is in keeping with the mean antenna separation along the arms of about 2.5 km, implying an approximate Nyquist sampling limit of 5 km. Because of this, we consider these spectra most reliable for $|k_{proj}| < 1.26 \text{ km}^{-1}$.

We note that for most of these one-hour mean spectra, the relatively small-scale ($|k_{proj}| > 0.1$) portions of the spectra that are above the noise level are roughly consistent with what is expected for E_s layers. From the data presented by *Coker et al.* [2009], a typical time series of E_s activity would yield values for the spectral power ranging from about 10^{-4} up to $10^{-3} \text{ mTECU}^2 \text{ km}^{-2} \text{ hr}^2$. This is nearly exactly the range inhabited by the intermediate/small-scale regions of the one-hour mean spectra plotted in Fig. 8. In addition, the contemporaneous ionosondes data presented in §3.3.2 and Fig. 6 show that E_s layers were likely present during the VLA observations.

For the remainder of the analysis, we found it useful to define three size classes for the detected waves: (1) medium scale, $|k_{proj}| < 0.1 \text{ km}^{-1}$ which includes the full range of MSTID sizes, (2) intermediate scale, $0.1 < |k_{proj}| < 0.3 \text{ km}^{-1}$, which represents the remaining range of scales one can probe with our previous polynomial-based approach, and (3) small scale, $0.3 < |k_{proj}| < 1.26 \text{ km}^{-1}$ representing the scales that cannot be probed with the polynomial fits.

We have re-displayed the arm-based spectra in Fig. 9 with these three size classes marked. In this representation, we have divided the spectra by an estimate of the spectra of background fluctuations, i.e., those that do not move in a preferred direction. We have estimated this background at each value of $|k_{proj}|$ and time step using a combination of the spectra from all three arms. In this process, only one of the two directions, up or down the arm, was used for each arm. In each case, the direction with the lowest power was used as it was more likely to be dominated by isotropic fluctuations. The median power among all three arms (within ± 1 pixel in both time

and $|k_{proj}|$) was then taken to be the value for the background. For displaying purposes only, we also applied a three-pixel square median filter to the arm-based spectra and divided these by the estimated background spectra and have shown them in Fig. 9. In this representation, one can see that groups of waves at virtually all detectable scales are seen moving in a variety of preferred directions at different times.

4.2. Group Wave Properties

To exploit the arm-based spectra described above and displayed in Fig. 7–9 to identify groups of waves moving in a particular direction, we have developed the following method. To begin, we computed a weighted mean value of k_{proj} for each size class, arm, and one-minute interval using the spectral power as the weight. If there is a significant population of waves within any of the three classes at a particular time step moving in a similar direction, these weighted mean values will follow a cosine as a function of the azimuth angle of the arms which will peak in the direction of the true wavenumber vector, \vec{k} .

To detect such groups of waves, we have fit a simple cosine model to the weighted mean k_{proj} values at each time step, including the nearest two time steps so that the fit would be better constrained and so some level of temporal coherence would be imposed. We then compared the amplitude of the fitted cosine with the rms scatter about the fit among the nine values used (i.e., three arms and three time steps) to assess the significance of the detection of a group of waves. We have plotted the azimuth angles for \vec{k} for both 3σ and 5σ detections for each of the three size classes in the panels of Fig. 10. The 5σ detections for the medium and intermediate scale waves have been re-plotted in the panels of the smaller size class(es) for comparison. For reference, we have also shaded in grey time ranges where MSTIDs were detected using the polynomial-based technique as described in §3.

In general, the \vec{k} directions for the medium-scale class agree with those seen for the detected MSTIDs displayed in Fig. 2, which serves to partially validate our arm-based method. Most of the time, the azimuth angles for the intermediate and small classes roughly agree, indicating that they are likely part of the same distribution of waves. Both often agree with the azimuth angles determined for the medium class, but are at times significantly different, most

notably during two instances where MSTIDs were detected.

We have also determined approximate speeds for all of the detected groups of waves which we have plotted in Fig. 11 with their values of $|\vec{k}|$ taken from the above described cosine fits. The speeds were computed using the mean temporal frequency within bins of k_{proj} that were within $\pm 0.1 \text{ km}^{-1}$ for the small class and $\pm 0.05 \text{ km}^{-1}$ for the intermediate and medium classes of the cosine fit-determined value of $|\vec{k}|$ from each arm. A spline fit to the data as a function of arm azimuth angle was then used to estimate the mean temporal frequency along the direction of \vec{k} where waves, rather than background fluctuations, are more likely to dominate. The speed was then computed using this frequency and the value of $|\vec{k}|$ from the cosine fit. The speeds agree in general with what can be seen in Fig. 10, that the medium-scale class of waves are a somewhat distinct population in terms of direction and speed whereas the intermediate and small scale classes tend to have similar directions and speeds.

4.3. Small-scale Waves

To further explore the nature of the small-scale waves in particular, we have plotted the distribution of azimuth angles for the 5σ detections in Fig. 12 for the small-scale class only. From this it can be seen that the distribution has four distinct peaks at angles of roughly -155° , -135° , 55° , and 120° . For reference, we have also plotted the azimuth angles of the three VLA arms (both up and down the arms) as vertical dashed lines. From this, one can see that the group of waves with a peak azimuth angle of 55° were moving almost directly up the southwestern arm. This indicates that this group of waves is likely small in extent as well as in wavelength. This is because for groups of waves substantially smaller than the array, the arm-based method we described above will be biased toward waves traveling along one of the three arms because the number of antennas that “see” these waves will be maximized in this case.

In contrast, groups of waves which span all or nearly all of the array will essentially be seen by all the antennas for any direction and will experience no such bias. This appears to be the case for the group of waves moving roughly southeastward and for the waves with a peak azimuth angle of -155° . The peak of the distribution for the southeastward-directed waves is somewhat skewed toward the az-

imuth of the southeastern arm. However, the bulk of these waves have azimuth angles between that of the southeastern (up) and northern (down) arms, indicating that any influence of the arm-based bias on these waves is minimal. The group of waves moving toward an angle of -135° peak near but not at the azimuth angle of the southwestern arm, indicating that their measured distribution has been influenced by the arm-based bias, but to a lesser degree than those whose distribution peaks near 55° .

Because of this bias, the paucity of waves directed either due west or east only indicates that there were few groups of small-wavelength waves moving in these directions which also spanned the array. However, the lack of small-scale waves seen directed northwest, due north, or due south (i.e., up the southeastern arm or up/down the northern arm) indicates a genuine absence of such phenomena and demonstrates that the population of small-scale waves was far from isotropic.

In terms of the implied orientation of the wavefronts, the peaks at -135° and 55° are essentially the same since they are roughly 180° apart. They are both conspicuously close to the required orientation for the E_s layer instability (or, “ E_s LI”) described in detail by *Cosgrove and Tsunoda* [2002]. They demonstrated that an E_s layer is unstable against perturbations with wavefronts aligned from northwest to southeast. In particular, for no meridional wind component, the optimum orientation is 35° west of magnetic north. For the VLA, where the magnetic declination is about 10° , this corresponds to k azimuth angles of either -115° or 65° . If there is a significant meridional wind component, the optimum angle can be as much as 15° closer to due south, giving a range of optimum position angles of -130° to -115° or 50° to 65° . This is roughly consistent with the locations of the two largest peaks in Fig. 12. However, the exact peak azimuth angles of these two distributions are not precisely constrained given the bias toward the direction of the VLA arms described above. We can only say that they are generally moving either northeast or southwest.

To illustrate the agreement with the predictions of the E_s LI model, we have computed the azimuth angle (at the VLA) dependence of the E_s LI assuming a magnetic dip angle of 45° according to *Cosgrove and Tsunoda* [2002], including a range of peak azimuth angles of 15° . We have plotted a scaled version of the growth rate in Fig. 12. From this curve, one can see that the bulk of the two groups of waves

with azimuth angles near the optimum values for the E_s LI are contained within the regions that are within $\sim 1/2$ of the maximum growth rate.

If we consider only those waves located in time ranges where MSTIDs were detected, the agreement with the predictions of the E_s LI growth rate are even better (see the red histograms in Fig. 12). In fact, only a small fraction of such waves ($\sim 2\%$) have azimuth angles where the E_s LI growth rate is ≤ 0 . In contrast, for all waves, about 16% lie outside this region. One can see from the red histograms in Fig. 12 that the azimuth angle distribution for the southwest-directed waves coincident with MSTIDs is significantly skewed with a tail extending away from the azimuth angle of the southwestern VLA arm. This indicates that the arm-based bias discussed above has a larger effect on these waves than the other southwest-directed waves which are not seen with MSTIDs and have a more symmetric distribution. This further implies that these groups of waves and their northeast-directed counterparts are relatively small in extent as compared to the other detected groups of small-scale waves.

We note that small-scale waves were detected during nearly all observed instances of MSTIDs. This indicates that the preference for small-scale waves aligned northwest to southeast during MSTID activity is not simply a product of the arm-based bias. In other words, there is no indication that there were periods of MSTID activity where small-scale waves were not detected because they were not directed along a VLA arm and their extent was too small to be detected with the arm-based method. This preference for northwest to southeast aligned, small-scale waves is again consistent with the notion that these waves are associated with the E_s LI. This is because according to *Cosgrove and Tsunoda* [2004], the coupling between the Perkins instability in the F region and the E_s LI is itself unstable.

The growth rate for the coupled instability is maximized for instances where both the F and E_s layer perturbations are aligned from northwest to southeast. From Fig. 10, we can see that while the small-scale waves are so aligned, the MSTIDs are not necessarily. However, we note that the range of allowed orientations for the Perkins instability is much broader than that for the E_s LI as it depends somewhat on the strength and orientation of the F region neutral wind.

We also note that models of this instability [*Yokoyama et al.*, 2009; *Yokoyama and Hysell*, 2010] have shown that random perturbations within an E_s layer are enough to form MSTIDs in the lower/bottom part of the F region through the E - F coupling mechanism. The MSTIDs can then, through this same coupling, help northwest to southeast aligned perturbations grow within the E_s layer. *Yokoyama et al.* [2009] confirmed that this process works most efficiently when conditions are right in the lower/bottom part of the F region to form northwest to southeast aligned MSTIDs. However, they also showed that while weaker, MSTIDs of different orientations (in their example, aligned north to south) could be formed through this process. In this case, the E_s layer waves that formed were still aligned northwest to southeast due to the more rigid directional constraints of the E_s LI. Therefore, the results show here are quite consistent with the predictions of E - F coupling in the nighttime, midlatitude ionosphere.

The group of small-scale waves seen in Fig. 12 to have \vec{k} pointed to the southeast cannot be explained with the E_s LI. However, several authors have noted that QP echoes are often found with no preferred direction, or with directions inconsistent with the direction-dependent E_s LI [e.g., *Fukao et al.*, 1998; *Yamamoto et al.*, 2005; *Larsen et al.*, 2007]. *Yamamoto et al.* [2005] found a tendency for the fronts of QP echoes to be nearly perpendicular to the direction of the neutral wind at the height of the E_s layer(s). To explore this possibility, we have plotted the neutral wind velocity azimuth angle profile taken from publicly available GPI data-driven runs of the TIEGCM code [*Wang et al.*, 1999, currently available at <http://www.hao.ucar.edu/modeling/tgcm/>] for the night of 13 August at 32.5°N and 110°W at one hour intervals in Fig. 13. In each panel, the \vec{k} azimuth angles of each 5σ detection of small-scale waves within the corresponding time bin is plotted as a vertical dotted line.

To form and maintain an E_s layer, a zonal wind shear is required with the westward moving wind at higher altitudes than the wind moving eastward. In the plots in Fig. 13, this occurs at altitudes where the neutral wind transitions from moving southeastward at lower altitudes to moving southwestward at higher altitudes. This usually occurs at heights between about 100 and 110 km which is typical for E_s layers. The small-scale waves detected with \vec{k} toward the southeast are then consistent with having wave-

fronts nearly perpendicular to the neutral wind at the E_s layer. We also note that the waves with \vec{k} pointing to the southwest which are not coincident with MSTIDs may also be consistent with this same scenario, depending on the altitude at which the proposed E_s layer has formed.

Yamamoto et al. [2005] concluded that these types of QP echoes may be formed either by interactions with gravity waves or via the Kelvin-Helmholtz instability. Since these waves were detected during the period of lowest MSTID activity (see Fig. 10 and 12), E - F coupling likely has little to do with the generation of these structures. Gravity waves or Kelvin-Helmholtz instabilities are much more likely candidates for their generation mechanism.

4.4. Background Fluctuations

While our arm-based techniques have found evidence for groups of waves moving in preferred directions on all size-scales, these results do not exclude the existence of populations of structures moving in a wide enough range of directions as to appear isotropic within our analysis. To examine this possibility, we have looked to the background spectra constructed using the arm spectra described in §4.1. These spectra should be reasonably free of the presence of directed waves and will provide insights into the quasi-isotropic set of background fluctuations. Mean background spectra computed within one hour bins are plotted in Fig. 14.

While some of these spectra may be reasonably approximated with single power-laws, many have the appearance of “broken,” or two-component power-laws. Upon detailed inspection, we found that both the inner and outer most regions of the spectra were roughly $\propto k^{-5/3}$, but with different slopes and offsets. This is intriguing since this is the dependence one expects for turbulent fluctuations. In particular, for a thin shell, *Tatarski* [1961] predicted from *Kolmogorov* [1941a, b] that the spectrum of refractive index fluctuations gives a spectrum of wavefront phase variations $\propto k^{-11/3}$. Since we have examined the gradient of TEC (or, wavefront phase) fluctuations, the fluctuations have been effectively multiplied by a factor of $i|\vec{k}|$, and so the power spectrum is altered by a factor of k^2 , or $\propto k^{-5/3}$. Thus, the general shapes of the background spectra suggest they may be interpreted as the sums of two separate turbulent components.

We have consequently fit a two-component turbulent model to each of the background spectra plotted in Fig. 14. To allow each spectrum to flatten above a maximum turbulent scale-length, λ_{max} , we assumed the following form for each component

$$\Psi(k) = \left[k^2 + \left(\frac{2\pi}{\lambda_{max}} \right)^2 \right]^{-\frac{5}{6}} \quad (4)$$

The resulting two-component fits are plotted with the spectra in Fig. 14; the two components are plotted separately as well. In general, one can see that each spectrum is well represented by a component with a relatively large λ_{max} (blue curves) and one that flattens at much smaller scales (higher wavenumbers; green curves). To illustrate this quantitatively, we have plotted in Fig. 15 the power at λ_{max} (upper panel) and λ_{max} (lower panel) for each of the two components as functions of local time. For both components, λ_{max} varies somewhat with time, but is typically ~ 300 km for the larger-scale turbulent component and roughly 10 km for the smaller-scale component. While the power at λ_{max} seems relatively stable with time for the larger component, the small-scale component shows a definite peak at a local time of about $-00^{\text{h}}30^{\text{m}}$. This corresponds to the middle of the roughly three-hour lull in MSTID activity that started around -02^{h} . Since we also detected small-scale waves consistent with QP-echoes generated by gravity waves during this time, it is possible that this increase in power is the result of the same gravity waves influencing turbulent processes in the lower ionosphere/thermosphere where the role of ion-neutral coupling is relatively strong.

5. Discussion

Our exploration of a long, VHF observation of Cyg A with the VLA has successfully demonstrated the power of this instrument to characterize a variety of transient ionospheric phenomena. For this observation, the typical 1σ uncertainty in the δTEC measurements was 3×10^{-4} TECU, yielding more than an order of magnitude better sensitivity to TEC fluctuations than can be achieved with GPS-based relative TEC measurements [see, e.g., *Hernández-Pajares et al.*, 2006]. Through our new spectral-based analysis, we have demonstrated the ability of the VLA to detect and characterize individual instances of MSTIDs as well as smaller-scale structures likely associated with E_s layers. We note that since disturbances

within the plasmasphere have been observed and in fact discovered with the VLA, it stands to reason that some of the phenomena we have detected may be located within the plasmasphere as well. However, the phenomena discovered by *Jacobson and Erickson* [1992b] have azimuth angles clustered around 102° (i.e., near magnetic east for the VLA), and few if any of the wave-like structures we have detected meet this criterion. Therefore, the vast majority (if not all) of the phenomena we have observed were likely within the ionosphere.

Among these phenomena are MSTIDs, small-scale wave-like phenomena consistent with E_s layer disturbances, and turbulent fluctuations. Both the MSTIDs and the small-scale fluctuations were present intermittently throughout the night, and turbulent fluctuations were seen at all times, which is common within VHF observations with the VLA [Cohen and Röttgering, 2009]. The MSTIDs appear to change direction after local midnight from being directed generally westward to being directed toward the northeast (see below). There is also a noticeable change in the turbulent activity near midnight, namely the spectral power of these fluctuations on small (~ 10 km) scales peaks near midnight and gradually decreases toward dawn.

5.1. West/northwest-directed MSTIDs

Before midnight local time, we observed instances of westward/northwestward moving MSTIDs (see Fig. 2) with an additional group moving westward observed briefly near $02^{\text{h}}30^{\text{m}}$ (see Fig. 10). While atypical for what is observed for most of North America [see *Tsugawa et al.*, 2007], the directions of these waves are similar to what is typically observed near the west coast in California during summer nighttime [see *Hernández-Pajares et al.*, 2006], especially those directed closer to due west.

Small-scale waves were detected coincident with nearly all of these MSTIDs moving toward either the northeast or southwest. Given the difference in directions, it is unlikely that these are simply the signatures of wavefront distortions within the MSTIDs themselves. As discussed above, the amplitudes and orientations of these small-scale waves are consistent with them being generated within E_s layers via the E_s LI. Coupling between the E_s LI and the Perkins instability in the F region [see *Cosgrove and Tsunoda*, 2004; *Cosgrove et al.*, 2004] may be what has influenced the MSTIDs observed near

dawn to move closer to northward as they were detected concurrently with northeastward-directed small-scale waves. In contrast, those waves seen near $02^{\text{h}}30^{\text{m}}$ were moving closer to due west and were accompanied by small-scale waves moving toward the southwest.

5.2. Northeastward-directed MSTIDs

Unusual, northeastward-directed MSTIDs were observed near 01^{h} to 02^{h} and 04^{h} to $04^{\text{h}}30^{\text{m}}$. As discussed above, *Shiokawa et al.* [2008] observed similar phenomena over Japan at midlatitudes during the night when the height of the F region was seen to drop significantly. Similarly, we have found evidence within data from relatively nearby ionosondes that suggests that the F region may have experienced a similar drop in height during the instances of northeastward-directed MSTIDs observed with the VLA.

Small-scale waves were also observed at the same times as these unusual MSTIDs. They were also mostly directed toward the northeast, suggesting that they may represent small-scale structures within the MSTIDs themselves. However, we note that (1) Fig. 11 shows that they were moving significantly more slowly than the MSTIDs, (2) the distribution of azimuth angles seen in Fig. 12 to peak near the azimuth angle of the VLA's southwestern arm indicates a bias that only affects groups of waves that span an area smaller than the array, and (3) toward the end of the night, the small-scale waves change direction toward the southwest while the MSTIDs remained northeastward directed. These factors seem to indicate that the small-scale waves are separate phenomena, similar to the other observed small-scale waves that are consistent with QP echoes generated within E_s layers. It could be that coupling between these disturbances and the larger waves in the F region plays some role in the unusual direction of the observed MSTIDs. In any case, a more thorough, statistical examination of these phenomena seems warranted.

5.3. Southeast/southwest-directed QP Echoes

There are two distinct groups of small-scale waves which were detected with no coincident MSTIDs. They were predominantly directed toward the southeast (from -02^{h} to 01^{h}) with a shorter period of activity of waves moving toward the southwest (between $-03^{\text{h}}30^{\text{m}}$ and $-02^{\text{h}}45^{\text{m}}$). The southeastward-

directed waves in particular seem to be somewhat different from the other observed small-scale waves. Given their orientations, they cannot have been generated via the E_s LI. They appear to be moving somewhat faster with typical speeds of about 150 m s^{-1} while most of the other small-scale waves have speeds between 30 and 100 m s^{-1} (see Fig. 11). They also seem to be largely unaffected by the arm-based bias discussed in §4.3, indicating that as a group, the likely span an area larger than that of the array.

Despite these differences, the southeastward-directed small-scale waves are generally consistent with QP echoes generated in E_s layers, both in amplitude and wavelength. They are more specifically consistent with the QP echoes observed by the Sporadic- E Experiments over Kyushu [SEEK *Fukao et al.*, 1998; *Yamamoto et al.*, 2005], which were heavily influenced by the direction of the neutral wind at the height of the E_s layer(s). The shift in direction at around $-02^{\text{h}}30^{\text{m}}$ from southwestward to southeastward may then be an indication of a change in E_s layer height from above the wind shear altitude to below it. This may imply the formation/dissipation of E_s layers near this time.

In addition, these waves occurred during the peak in small-scale turbulent activity as evidenced by the results shown in Fig. 15. This suggests that the same mechanism that generated these QP echoes also caused a significant turbulent disturbance in the lower ionosphere/thermosphere. Since the Rocky Mountains lie largely to the north and northwest of the VLA, this mechanism is likely gravity waves associated with wind flow over the Rocky Mountains.

Acknowledgments. The authors would like to thank the referees for useful comments and suggestions. Basic research in astronomy at the Naval Research Laboratory is supported by 6.1 base funding. The VLA was operated by the National Radio Astronomy Observatory which is a facility of the National Science Foundation operated under cooperative agreement by Associated Universities, Inc. Part of this research was carried out at the Jet Propulsion Laboratory, California Institute of Technology, under a contract with the National Aeronautics and Space Administration.

Notes

1. Since the wave properties are derived from the phases of the combined Fourier transform of several phenomena, the derived wavenumbers and pattern speeds are not strictly weighted mean values but are proportional to the phases of the weighted mean Fourier transform of the phenomena.

References

- Bernhardt, P. A., and C. L. Siefing (2006), New satellite-based systems for ionospheric tomography and scintillation region imaging *Rad. Sci.*, *41*, RS5S23
- Cohen, A. S., W. M. Lane, W. D. Cotton, N. E. Kassim, T. J. W. Lazio, R. A. Perley, J. J. Condon, and W. C. Erickson (2007), The VLA Low-Frequency Sky Survey *Astron. J.*, *134*, 1245–1262
- Cohen, A. S. and H. J. A. Röttgering (2009), Probing Fine-scale Ionosphere Structure with the Very Large Array Radio Telescope, *Astron. J.*, *138*, 439–447
- Coker, C., S. E. Thonnard, K. F. Dymond, T. J. W. Lazio, J. J. Makela, and P. J. Loughmiller (2009), Simultaneous radio interferometer and optical observations of ionospheric structure at the Very Large Array *Rad. Sci.*, *44*, RS0A11
- Cosgrove, R. B. and R. T. Tsunoda (2002), A direction-dependent instability of sporadic- E layers in the nighttime midlatitude ionosphere, *Geophys. Res. Lett.*, *29*, 18, 1864–1867
- Cosgrove, R. B. and R. T. Tsunoda (2004), Instability of the $E - F$ coupled nighttime midlatitude ionosphere, *J. of Geophys. Res.*, *109*, A04305
- Cosgrove, R. B., R. T. Tsunoda, S. Fukao, and M. Yamamoto (2004), Coupling of the Perkins instability and the sporadic E layer instability derived from physical arguments, *J. of Geophys. Res.*, *109*, A06301
- Dymond, K. F., C. Watts, C. Coker, S. A. Budzien, P. A. Bernhardt, N. Kassim, T. J. Lazio, K. Weiler, P. C. Crane, P. S. Ray, A. Cohen, T. Clarke, L. J. Rickard, G. B. Taylor, F. Schinzel, Y. Pihlstrom, M. Kuniyoshi, S. Close, P. Colestock, S. Myers, and A. Datta (2011), A Medium-Scale Traveling Ionospheric Disturbance Observed from the Ground and from Space, *Rad. Sci.*, *46*, RS5010
- Fukao, S., M. Yamamoto, R. T. Tsunoda, H. Hayakawa, and T. Mukai (1998), The SEEK (Sporadic- E Experiment over Kyushu) campaign, *Geophys. Res. Lett.*, *25*, 1761–1764
- Helmboldt, J. F., T. J. W. Lazio, H. T. Intema, and K. F. Dymond (2011), High-precision Measurements of Ionospheric TEC Gradients with the Very Large Array VHF System, *Rad. Sci.*, submitted
- Hernández-Parajes, M., J. M. Juan, and J. Sanz (2006), Medium-scale traveling ionospheric disturbances affecting GPS measurements: Spatial and temporal analysis, *J. of Geophys. Res.*, *111*, A07S11
- Hoogeveen, G. W. and A. R. Jacobson (1997), Improved analysis of plasmasphere motion using the VLA radio telescope, *Ann. of Geophys.*, *15*, 236–245
- Larsen, M. F., D. L. Hysell, Q. H. Zhou, S. M. Smith, J. Friedman, and R. L. Bishop (2007), Imaging coherent scatter radar, incoherent scatter radar, and optical observations of quasiperiodic structures associated with sporadic E layers, *J. of Geophys. Res.*, *112*, A06321

- Jacobson, A. R. and W. C. Erickson (1992a), A Method for Characterizing Transient Ionospheric Disturbances Using a Large Radiotelescope Array, *Astron. Astrophys.*, 257, 401–409
- Jacobson, A. R. and W. C. Erickson (1992b), Wavenumber-resolved Observations of Ionospheric Waves Using the Very Large Array Radiotelescope, *Plant. Space. Sci.*, 4, 447–455
- Kolmogorov, A. N. (1941a), The local structure of turbulence in incompressible viscous fluid for very large Reynold's numbers, *Dokl. Akad. Nauk SSSR*, 30, 301–305
- Kolmogorov, A. N. (1941b), Dissipation of energy in the locally isotropic turbulence, *Dokl. Akad. Nauk SSSR*, 32, 16–18
- Shiokawa, K., Y. Otsuka, N. Nishitani, T. Ogawa, T. Tsugawa, T. Maruyama, S. E. Smirnov, V. V. Bychkov, and B. M. Shevtsov (2008), Northeastward motion of nighttime medium-scale traveling ionospheric disturbances at middle latitudes observed by an air-glow imager *J. of Geophys. Res.*, 113, A12312
- Tatarski, V. I. (1961), *Wave Propagation in a Turbulent Medium*, McGraw-Hill, New York, New York ASP, San Francisco, Calif.
- Thompson, A. R., J. M. Moran, G. W. Swenson (1991), *Interferometry and synthesis in radio astronomy*, Krieger Pub., Malabar, Fla.
- Tolman, B., R. B. Harris, T. Gaussiran, D. Munton, J. Little, R. Mach, S. Nelsen, and B. Renfro (2004), The GPS Toolkit: Open Source GPS Software, paper presented at 16th International Technical Meeting of the Satellite Division of the Institute of Navigation, Long Beach, Calif.
- Tsugawa, T. Y., Y. Otsuka, A. J. Coster, and A. Saito (2007), Medium-scale traveling ionospheric disturbances detected with dense and wide TEC maps over North America, *Geophys. Res. Lett.*, 34, L22101
- Yamamoto, M., S. Fukao, R. T. Tsunoda, R. Pfaff, and H. Hayakawa (2005), SEEK-2 (Sporadic-*E* Experiment over Kyushu 2) – Project Outline, and Significance, *Ann. Geophys.*, 23, 2295–2305
- Yokoyama, T., D. L. Hysell, Y. Otsuka, and M. Yamamoto (2009), Three-dimensional simulation of the coupled Perkins and *E_s*-layer instabilities in the nighttime midlatitude ionosphere *J. of Geophys. Res.*, 114, A03308
- Yokoyama, T. and D. L. Hysell (2010), A new midlatitude ionosphere electrodynamics coupling model (MIECO): Latitudinal dependence and propagation of medium-scale traveling ionospheric disturbances *Geophys. Res. Lett.*, 37, L08105
- Wang, W., T. L. Killeen, A. G. Burns, and R. G. Roble (1999), A high-resolution, three-dimensional, time dependent, nested grid model of the coupled thermosphere-ionosphere, *J. Atmos. Sol.-Terr. Phys.*, 61, 385–397
- J. F. Helmboldt, US Naval Research Laboratory, Code 7213, 4555 Overlook Ave. SW, Washington, DC 20375 (joe.helmboldt@nrl.navy.mil)
- T. J. W. Lazio, Jet Propulsion Laboratory, California Institute of Technology, M/S 138-308, 4800 Oak Grove Dr., Pasadena, CA 91106 (joseph.lazio@jpl.nasa.gov)
- H. T. Intema, National Radio Astronomy Observatory, 520 Edgemont Rd, Charlottesville, VA 22903 (hintema@nrao.edu)
- K. F. Dymond, US Naval Research Laboratory, Code 7655, 4555 Overlook Ave. SW, Washington, DC 20375 (kenneth.dymond@nrl.navy.mil)

(Received _____.)

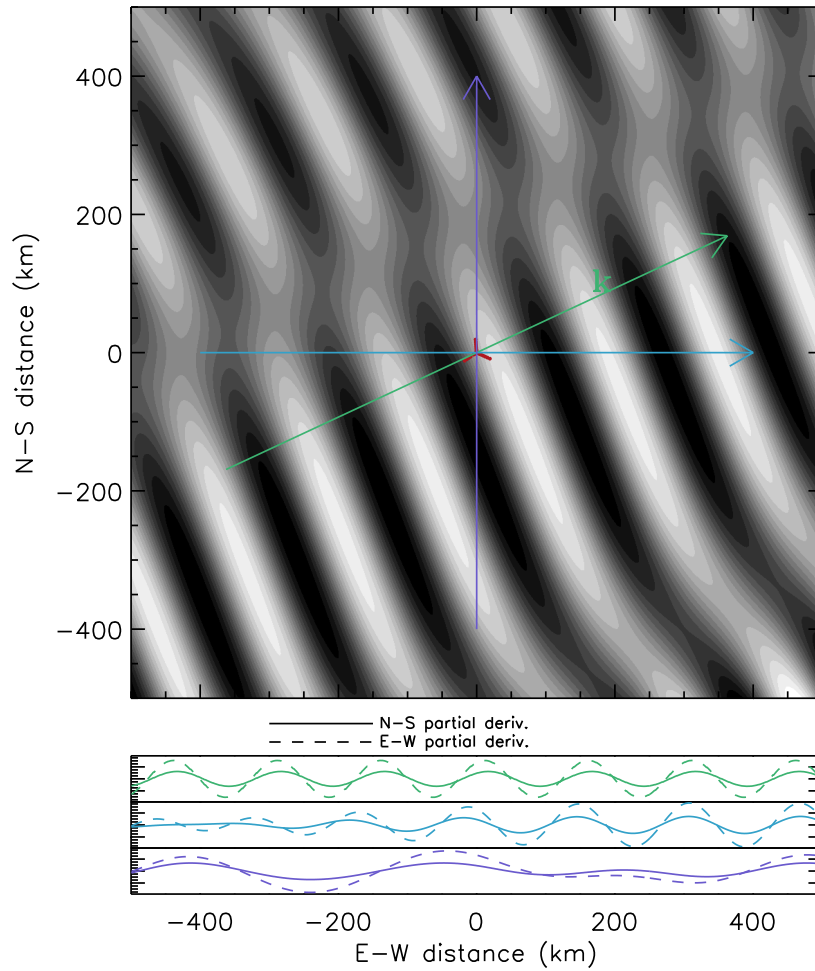


Figure 1. To illustrate the technique used to extract wave properties described in §3, an example of a wave, including wavefront distortions, that might be observed by the VLA (shown as a red “Y”). The lower panels show the N-S (solid line) and E-W (dashed line) partial derivatives along each of the vectors plotted in the upper panel.

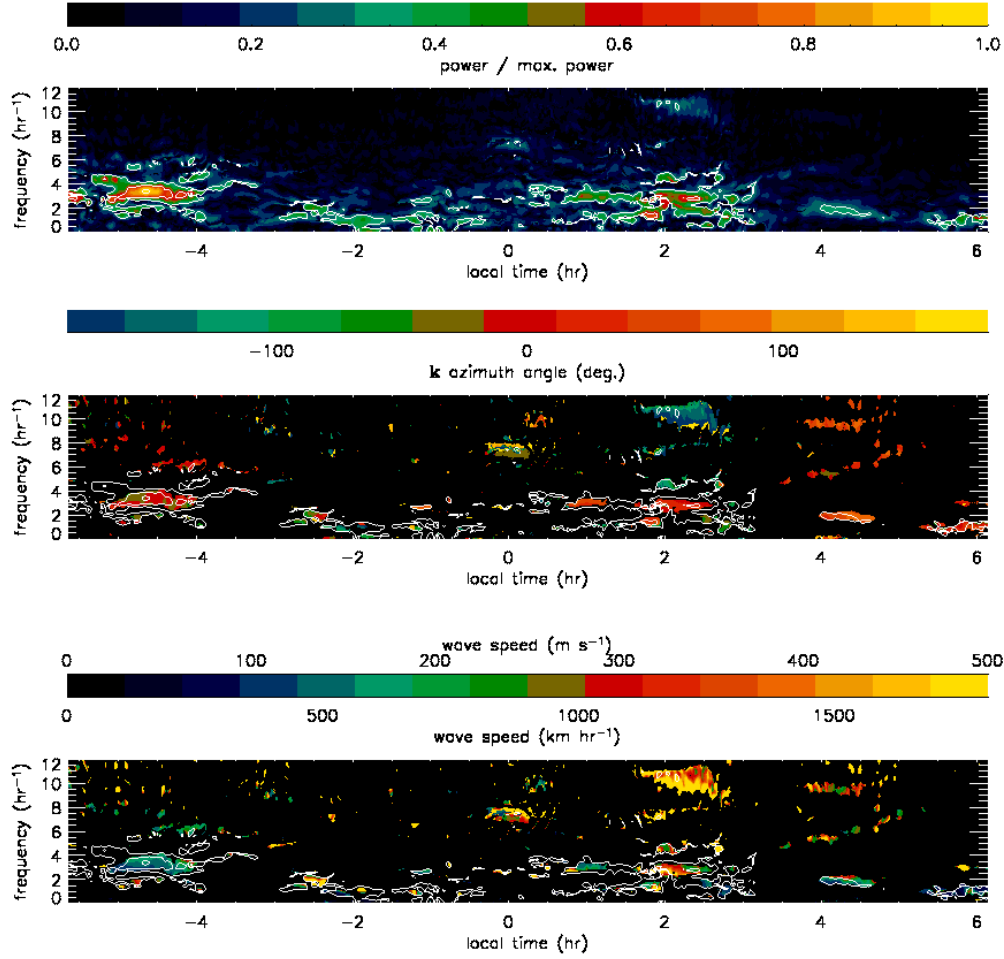


Figure 2. Upper: The power in the direction of the wavenumber vector, \vec{k} , as a function of local time (abscissa) and temporal frequency (ordinate) of Fourier modes within the δ TEC data. Middle: The azimuth angle of the wavenumber vector of each Fourier mode with power significantly larger than background levels (see §3.2). Lower: The velocity of each Fourier mode, using the same masking as in the middle panel. In all panels, the white contours are of spectral power.

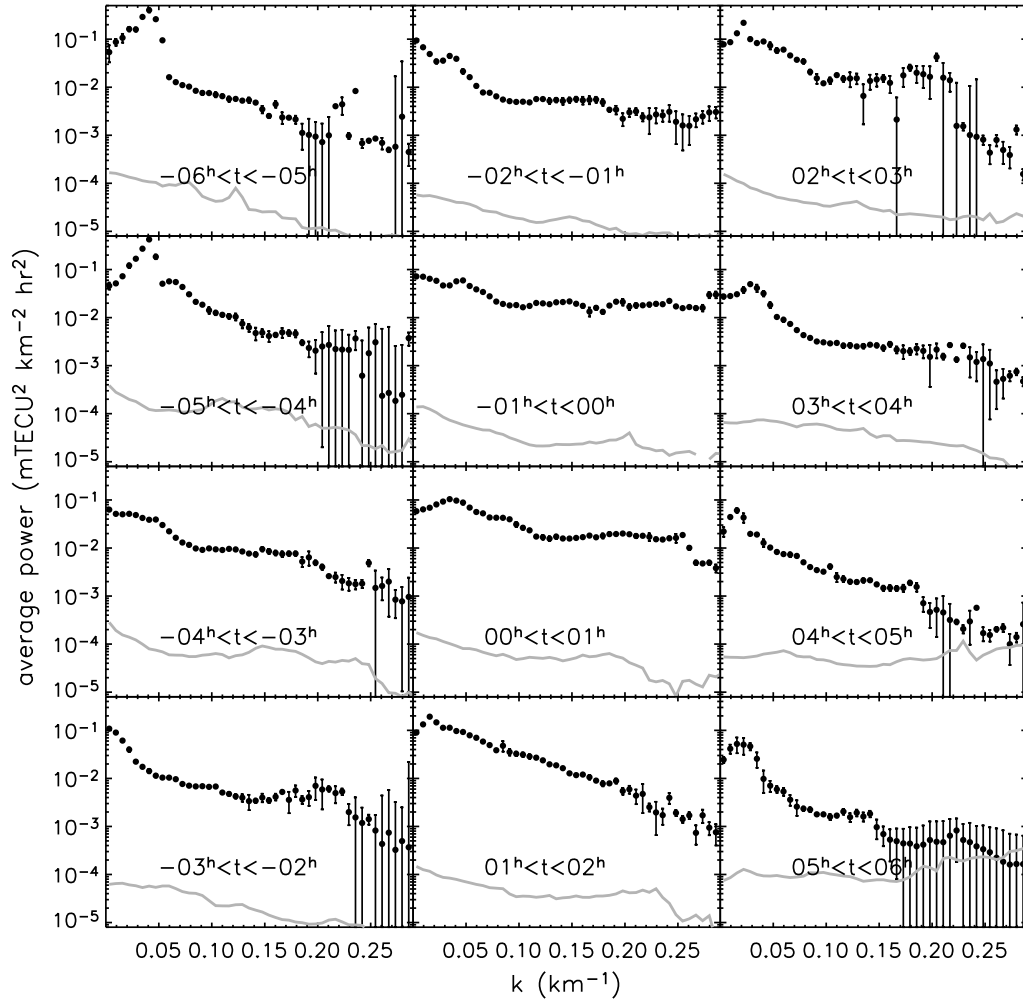


Figure 3. Within one-hour bins, the mean power as a function of wavenumber, k , for the data displayed in Fig. 2. The noise-equivalent spectra (see §3.3) are also plotted as grey curves.

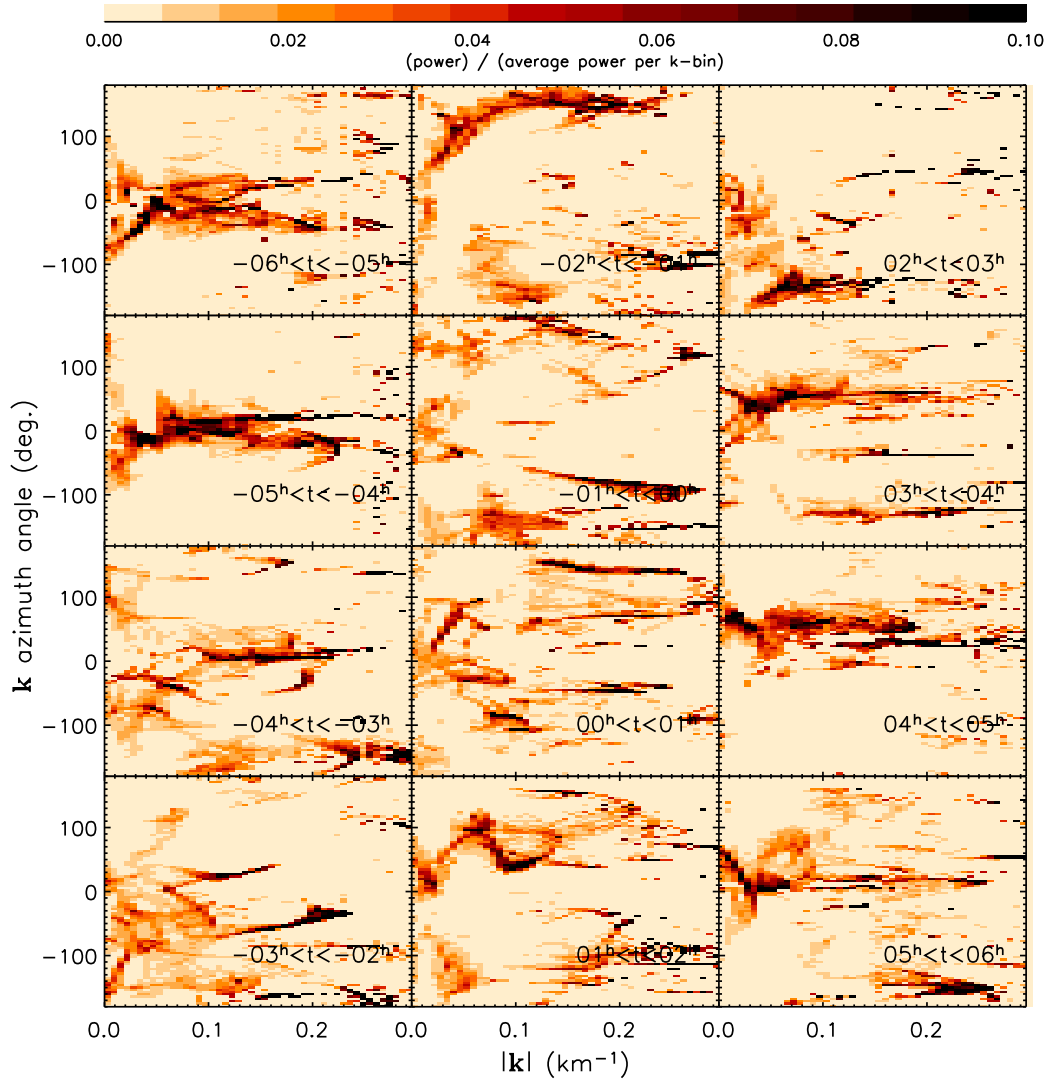


Figure 4. Within one-hour bins, the mean power within bins of wavenumber, k , and azimuth angle. The values within each bin have been normalized by the total power with all bins with the same wavenumber range to enhance the appearance of any detected features.

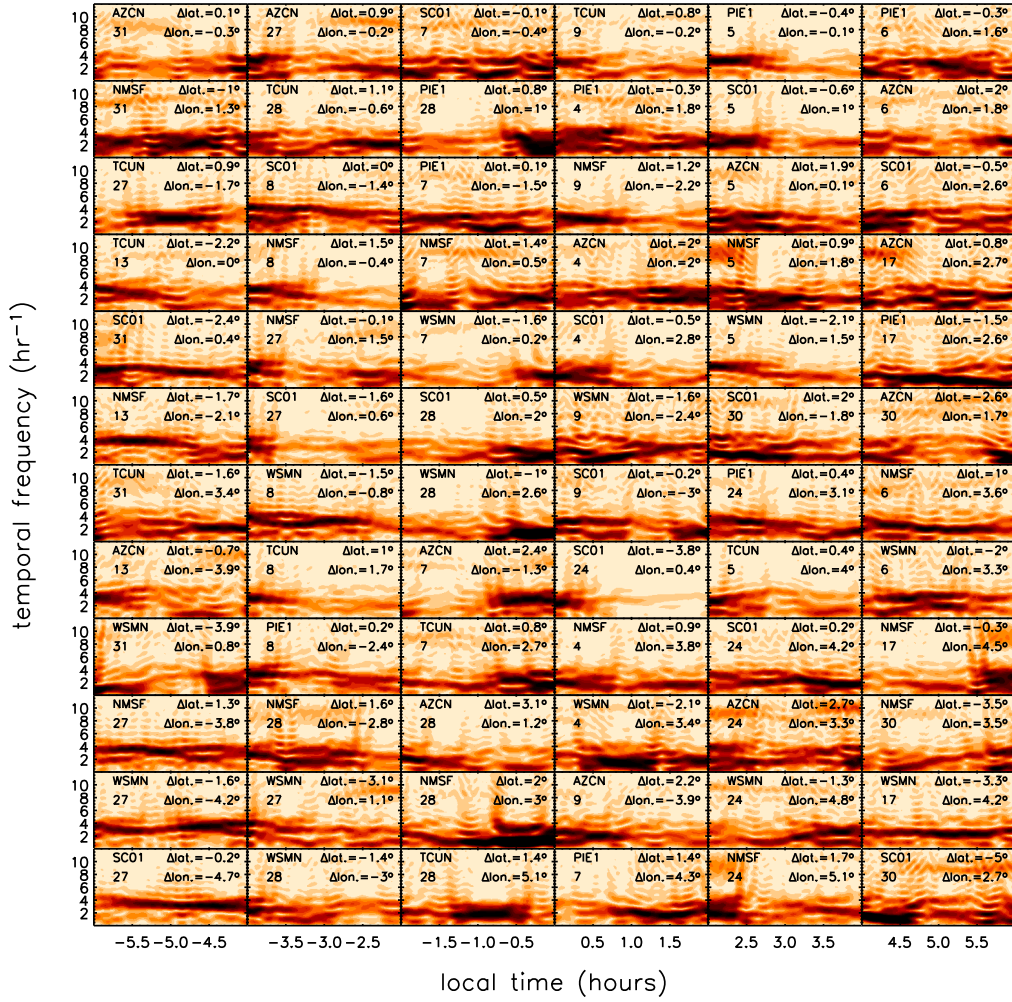


Figure 5. Fluctuation spectra as a function of local time and temporal frequency for contemporaneous GPS observations (see §3.4.1). Within each two-hour block, the spectra are sorted by the angular separation between their ionospheric pierce-points and that of Cyg A from top to bottom. In each panel, the station code and GPS satellite number are printed in the upper left and the pierce-point latitude and longitude relative to that of the Cyg A pierce point is printed in the upper right.

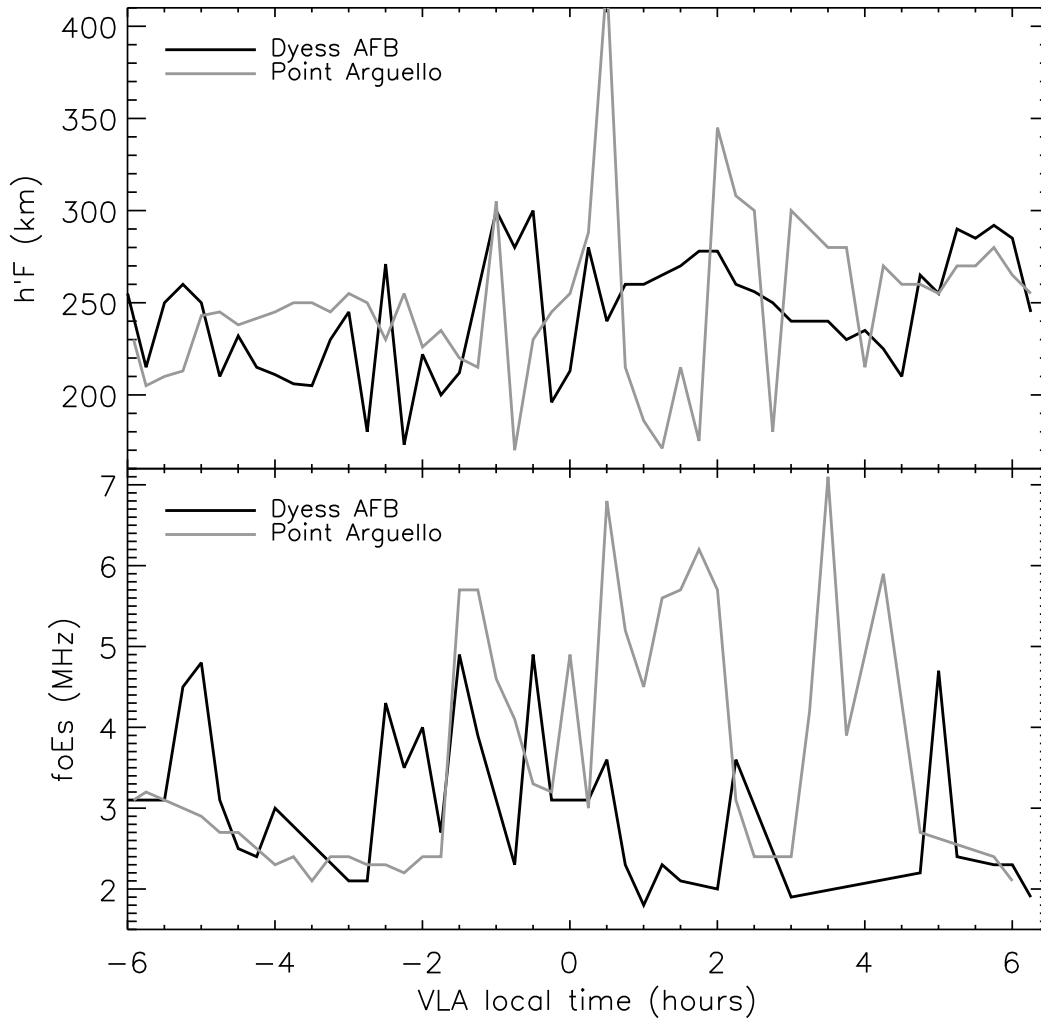


Figure 6. For two nearby ionosondes stations, Dyess Air Force Base ($32^{\circ} 30''$ N; $99^{\circ} 42'$ W) and Point Arguello ($35^{\circ} 36''$ N; $120^{\circ} 36'$ W), $h'F$ (upper) and $foEs$ (lower) as functions of VLA local time.

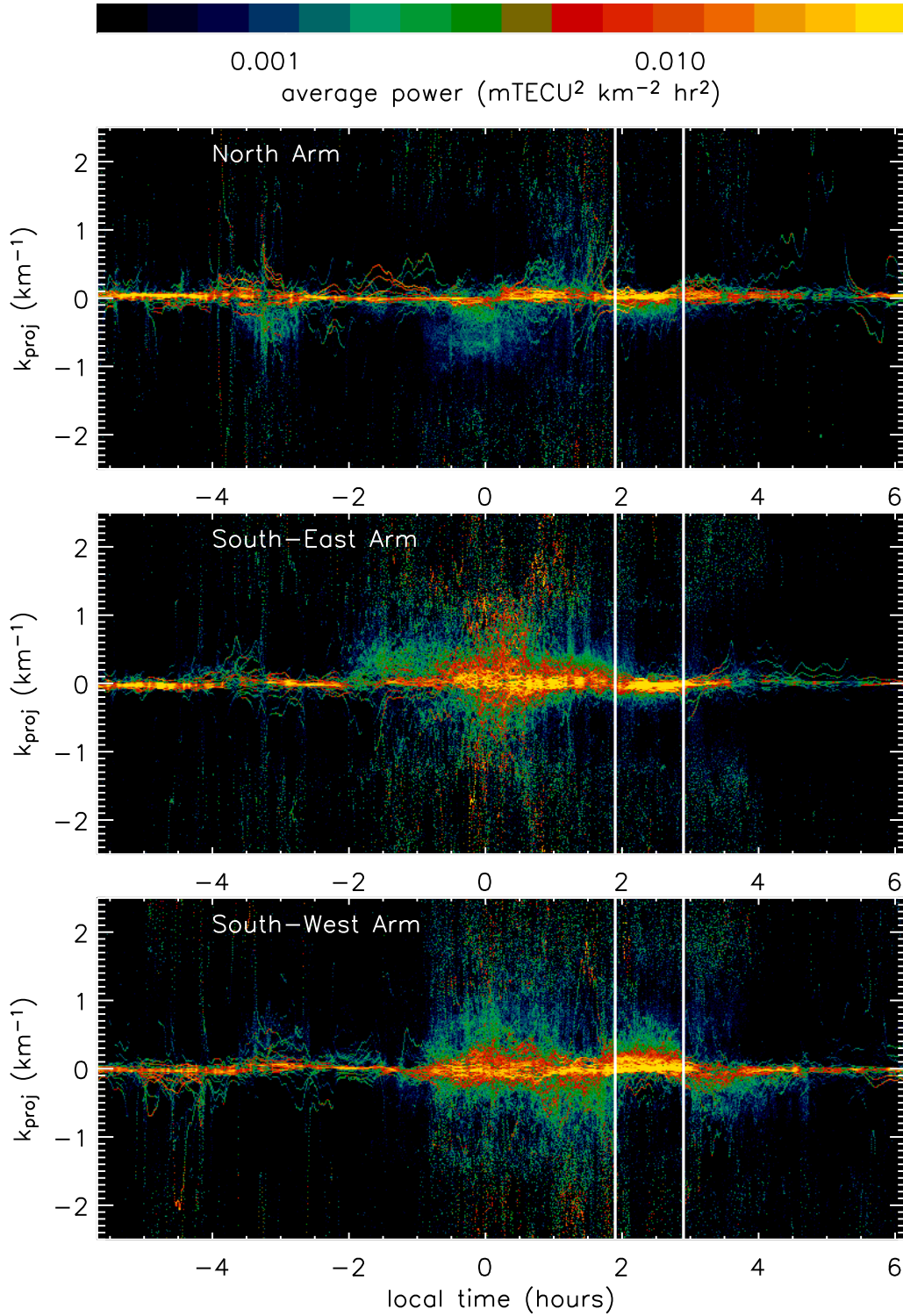


Figure 7. For each of the VLA arms, the total power as a function of projected wavenumber, k_{proj} , within one-minute bins. The region highlighted with vertical white lines in each panel is discussed in §4.1.

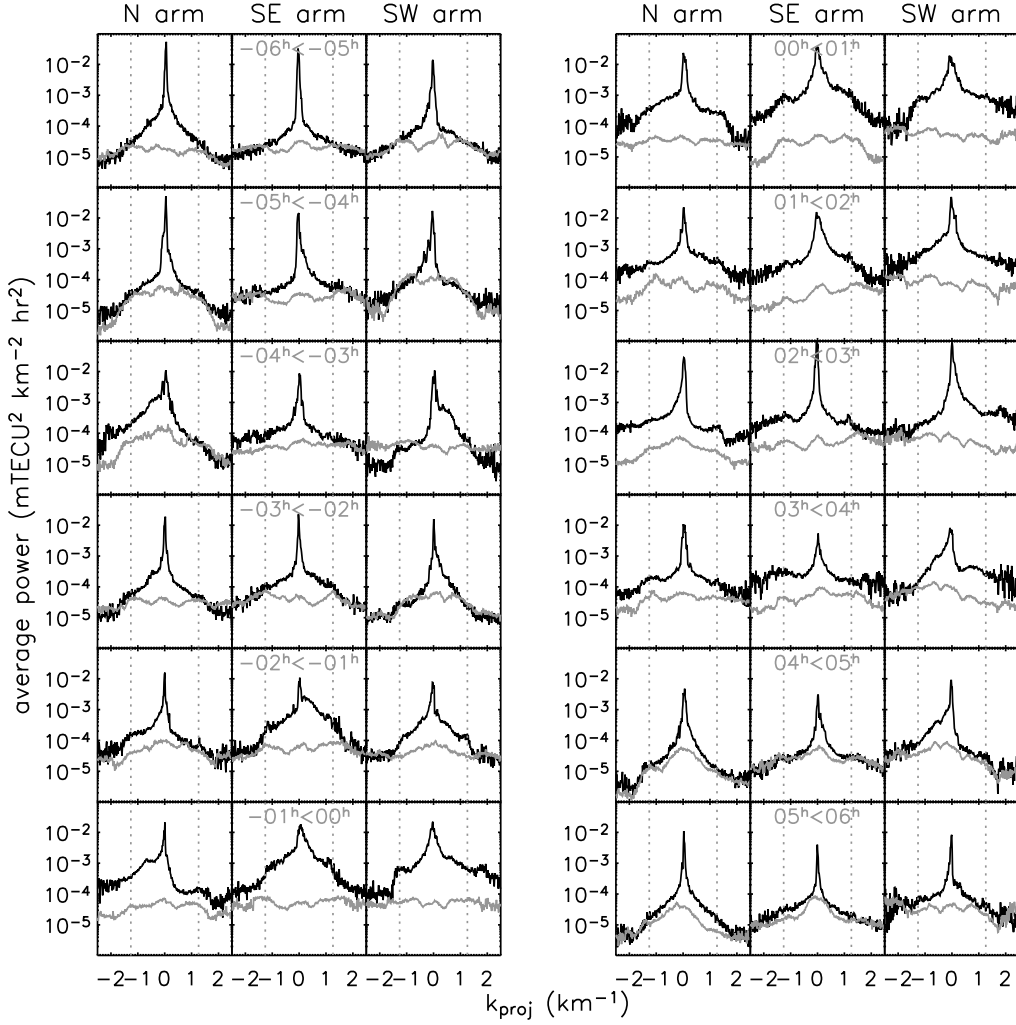


Figure 8. Within one-hour bins, the mean power within bins of projected wavenumber, k_{proj} , for each of the VLA arms. The noise-equivalent spectrum (see §4.1) is also plotted in each panel as a grey curve. The vertical dotted grey lines denote values of $k_{\text{proj}} = \pm 1.26 \text{ km}^{-1}$ which corresponds to the approximate Nyquist sampling limit for the average antenna separation of 2.5 km along the VLA arms (in A configuration).

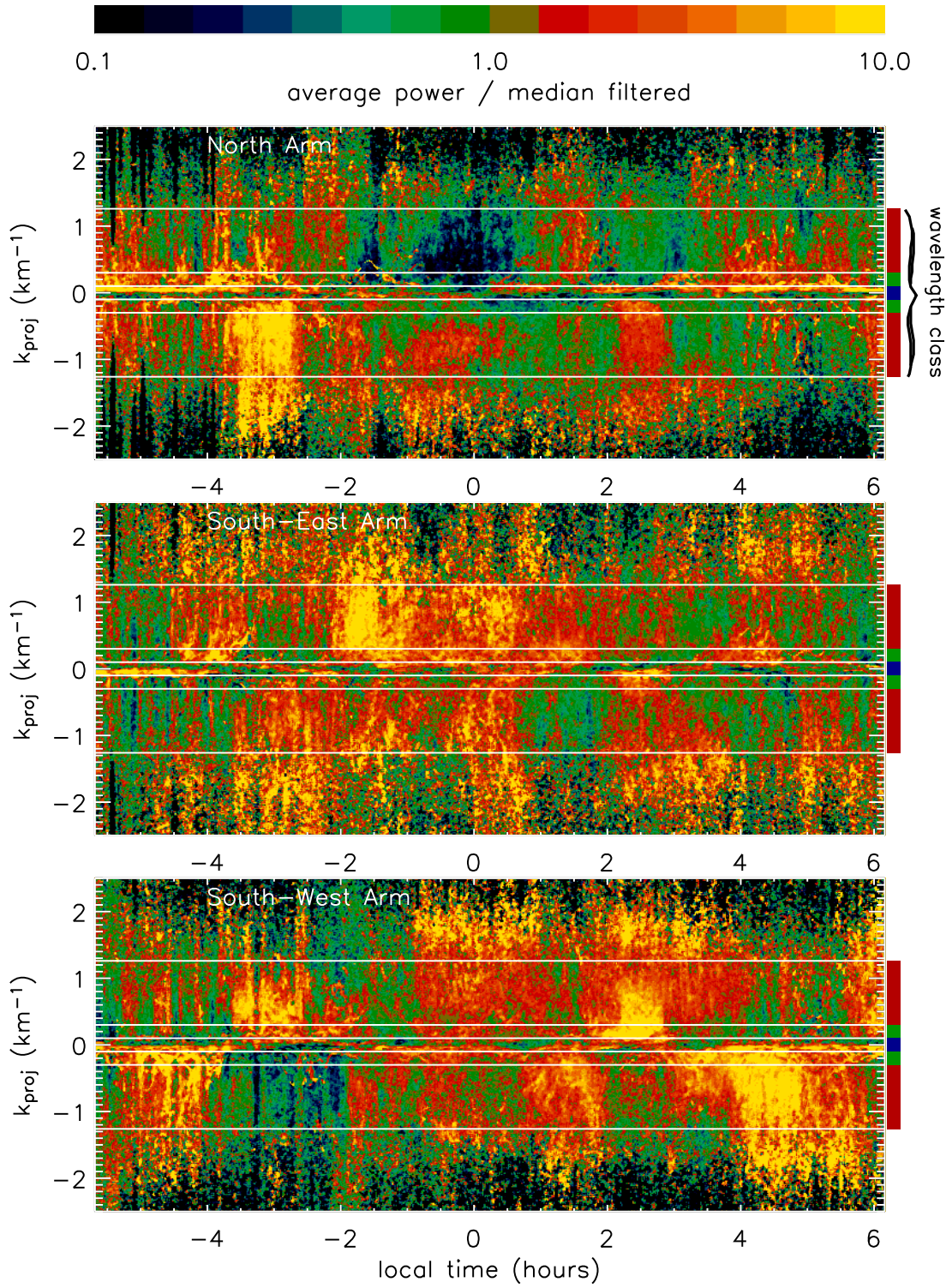


Figure 9. The spectra from Fig. 7 normalized by the estimated background spectrum and with the three wavenumber classes highlighted (see §4.1).

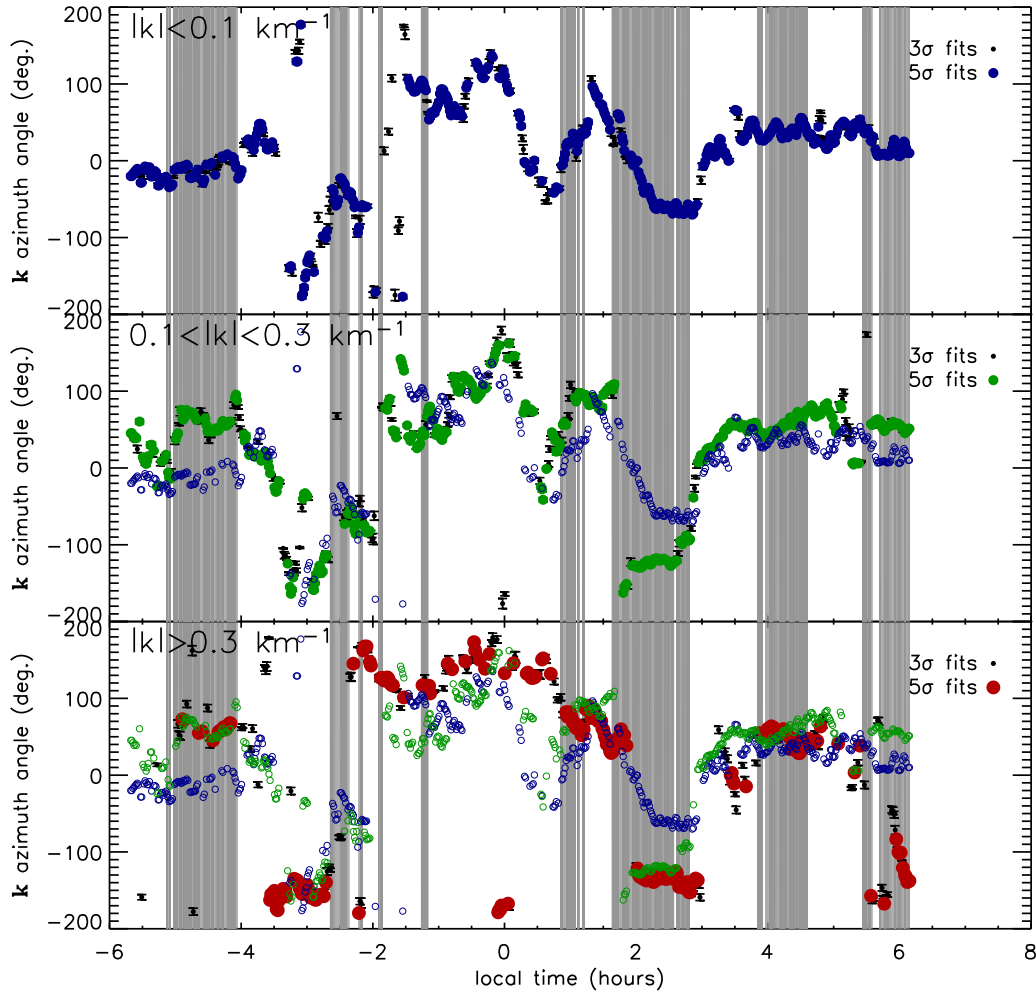


Figure 10. The wavenumber vector azimuth angle for 3σ and 5σ detections (see §4.2) for each of the three wavenumber classes. Time ranges where MSTIDs were detected from the data displayed in the upper panel of Fig. 2 are shaded in grey.

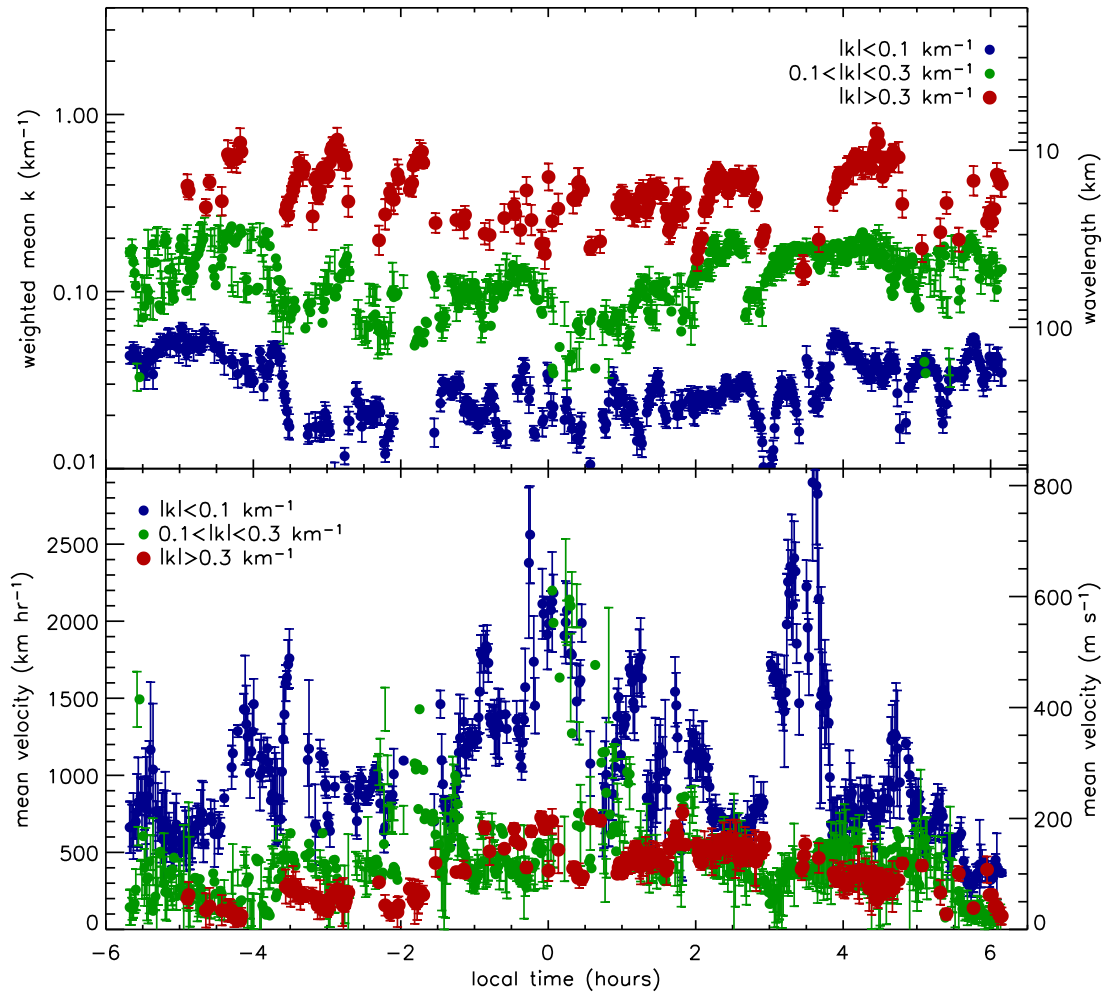


Figure 11. The weighted mean wavenumber/wavelength (upper) and velocity (lower) for 5σ detections (see §4.2) for each of the three wavenumber classes.

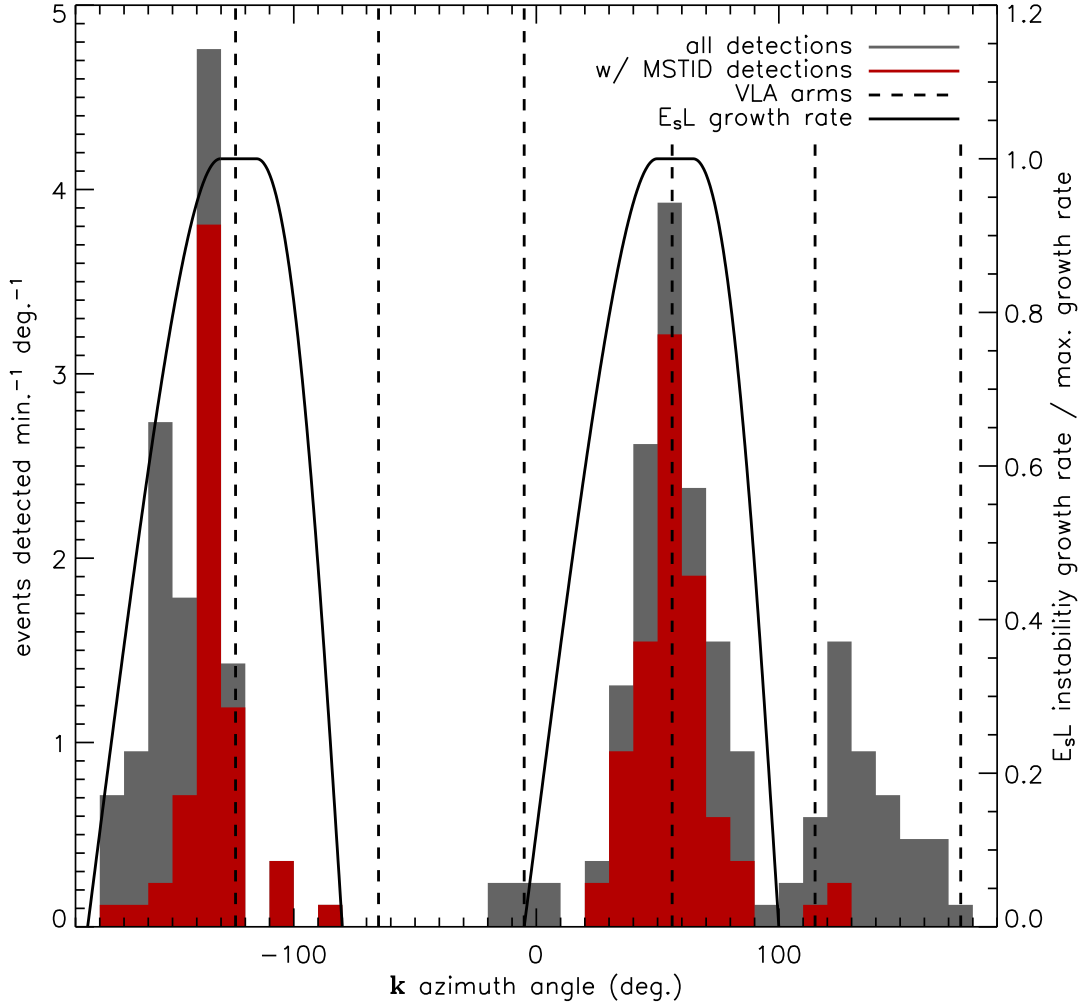


Figure 12. The distribution of \vec{k} azimuth angles for 5σ detections of small-scale moving structures displayed in Fig. 10 (shaded grey histograms). The same distribution for those detections that were coincident with MSTID detections (see Fig. 10) are displayed in red. The growth rate for the E_s layer instability is plotted as a black curve (see right ordinate for scale), allowing for a range in meridional wind components [see §4.3 and *Cosgrove and Tsunoda, 2002*].

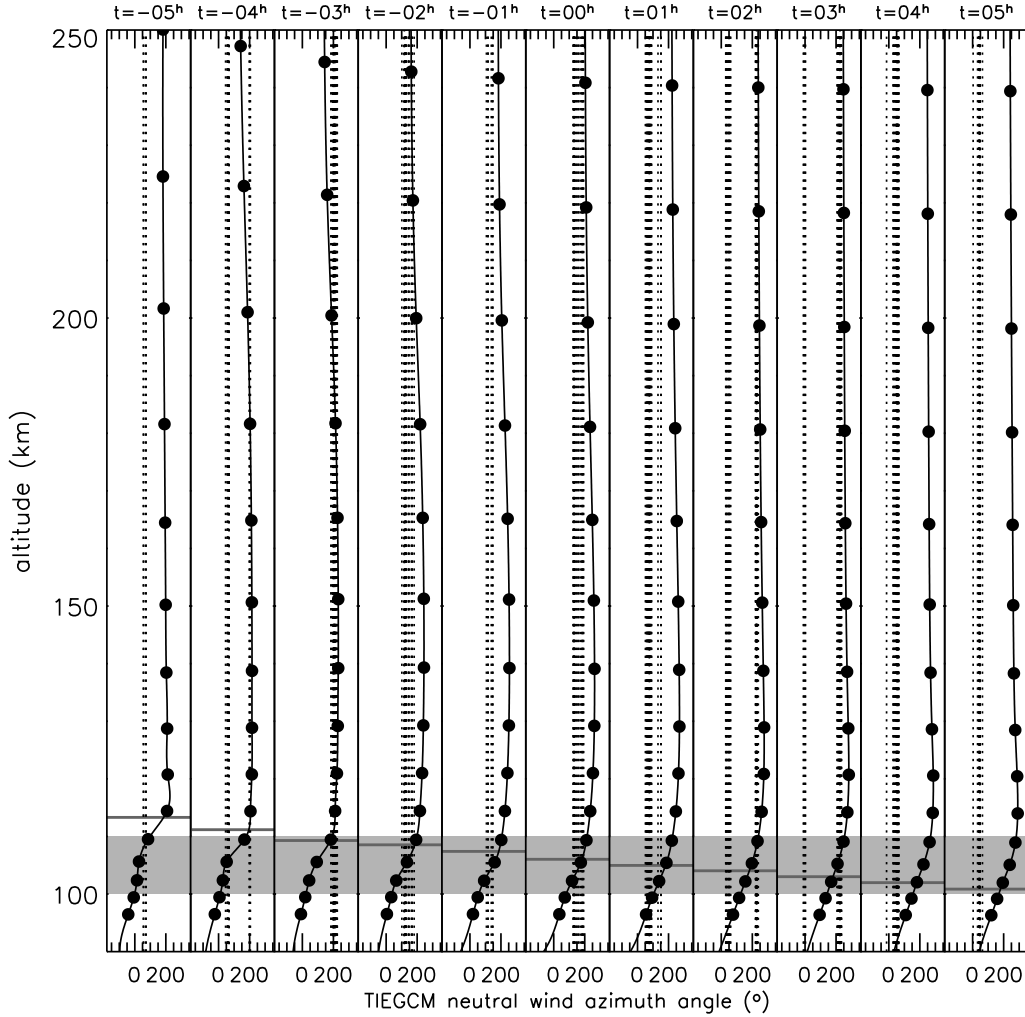


Figure 13. Within one-hour windows, the azimuth angle of the neutral wind velocity vector from TIEGCM as a function of altitude (points with cubic spline fits plotted as solid curves). In each panel, the vertical dotted lines represent the k azimuth angles for the 5σ detections of small-scale moving structures. The light-grey shaded regions indicate the typical range in altitudes for E_s layers, 100–110 km. Each dark-gray horizontal line indicates the altitude where the wind direction changes from eastward at lower altitudes to westward at higher altitudes, i.e., where the wind shear necessary for creating an E_s layer exists.

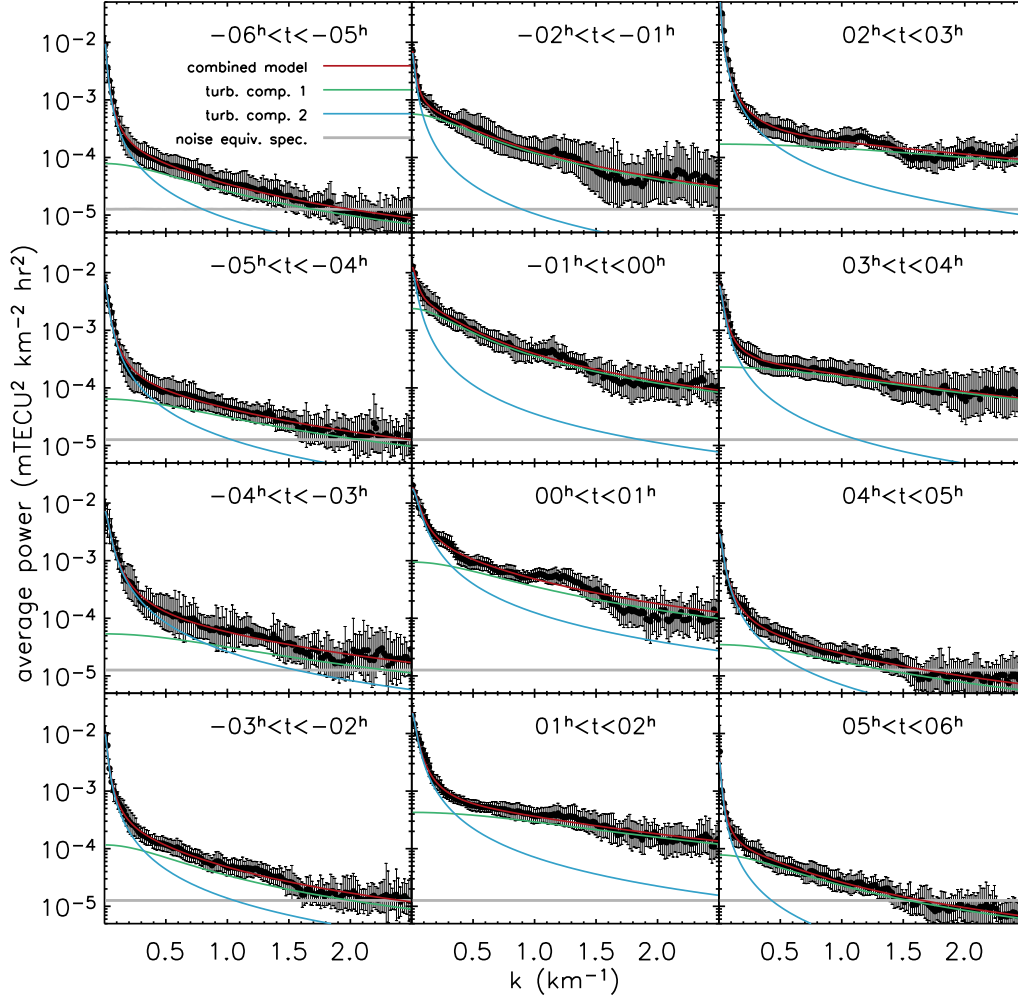


Figure 14. Within one-hour bins, the mean estimated background fluctuation spectra (see §4.1 and §4.4). The curves represent two-component turbulence fits to the spectra (see §4.4; component 1 is the smaller-scale component; component 2 is the larger-scale component). Noise equivalent spectra are plotted as grey curves.

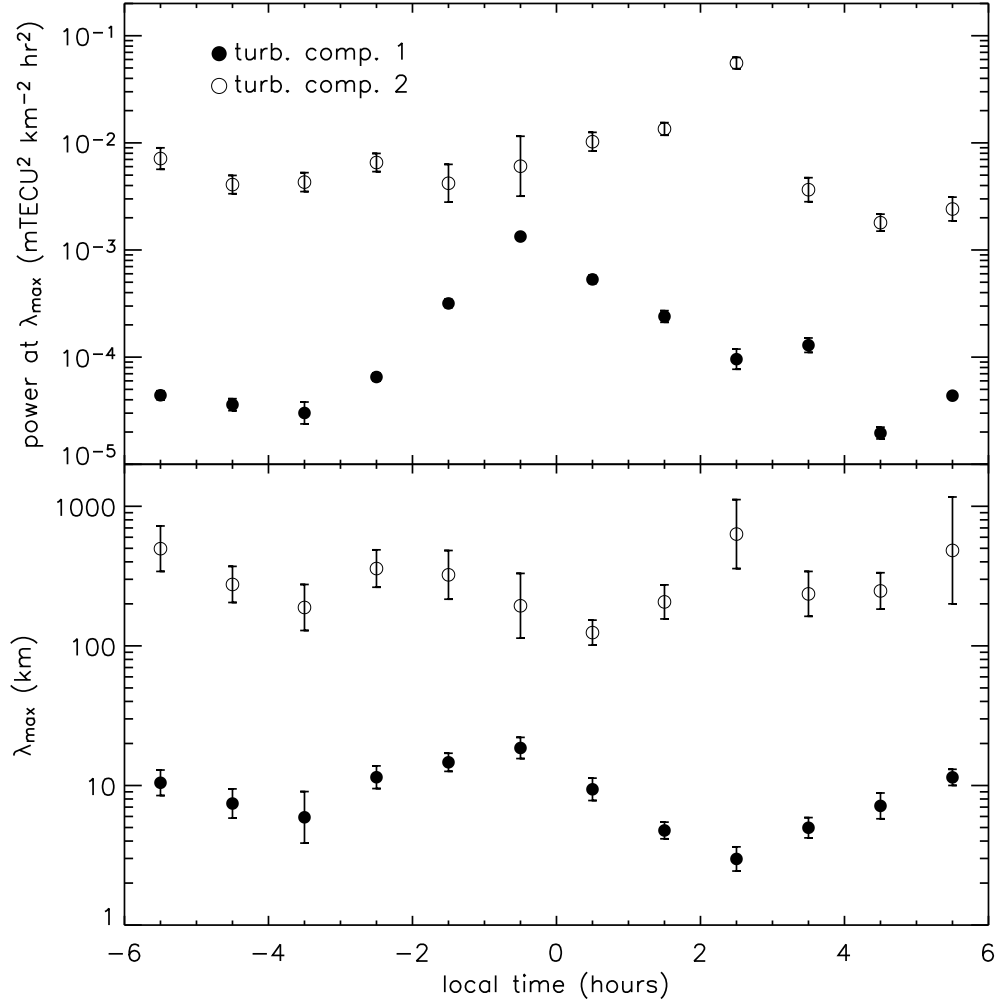


Figure 15. For the two-component turbulence fits displayed in Fig. 14, the power at the maximum wavelength (upper) and the maximum wavelength (lower) for each component as functions of local time [see §4.4 and equation (4)]. Here, turbulent component 1 (green curves in Fig. 14) refers to the smaller-scale turbulent component and turbulent component 2 (blue curves in Fig. 14) refers to the larger-scale component.